Universal Resonant Parameter Design Method Based on Multiple Boundary Constraints for Wireless Fast Charging

Yongbin Jiang, *Member, IEEE*, Yue Wu, *Student Member, IEEE*, Yaohua Li, *Student Member, IEEE*, Ning Wang, *Student Member, IEEE*, Xipei Yu, *Student Member, IEEE*, Xiaohua Wang, *Senior Member, IEEE*, and Yi Tang, *Senior Member, IEEE*

***Abstract*—Traditional resonant parameter design methods below MHz applications primarily rely on designer's experience and labor-intensive trial-and-error processes, which are not only time-consuming and inefficient but also fail to optimize system performance. This research proposes a universal resonant parameter design method based on multiple boundary constraints (MBCs) guiding engineers to complete the system design efficiently for wireless fast charging. This design method comprehensively considers multiple factors in parameter design and innovatively transforms them into constraint relationships, which are then mapped onto a 2-D plane graph to optimize the selection of self-inductances for the transmitting and receiving coils. Beyond rapidly generating an optimized coil design, this design method can also assist designers in refining unreasonable design specifications, significantly enhancing design efficiency and ensuring design results completely leverage superior system performance. According to experimental results, the coils developed with the MBCs-based method not only enable the WPT system to obtain outstanding steady-state and dynamic performance, but also result in high transfer efficiency. With a coupling coefficient k of 0.183 or 0.151, the maximum transfer efficiency can achieve 94.83% or 93.93% under the power rating of 1 kW as well as 91.25% or 87.87% under the power rating of 288 W (light load condition).**

***Index Terms*—Fast charging, multiple boundary constraints (MBCs), parameter design, wireless power transfer (WPT).**

Received 23 November 2024; revised 11 February 2025 and 20 April 2025; accepted 14 May 2025. Date of publication 26 May 2025; date of current version 27 August 2025. This work was supported in part by A*STAR under its Japan-Singapore Joint Call: Japan Science and Technology Agency (JST) and Agency for Science, Technology and Research (A*STAR) 2024 under Award R24I6IR134 and in part by the Ministry of Education, Singapore, under Grant Tier 1 RG73/24. Recommended for publication by Associate Editor X. Ruan. *(Corresponding authors: Xiaohua Wang; Yi Tang.)*

Yongbin Jiang, Yaohua Li, and Yi Tang are with the School of Electrical and Electronic Engineering, Nanyang Technological University, Singapore 639798 (e-mail: yongbin.jiang@ntu.edu.sg; yaohua001@e.ntu.edu.sg; yitang@ntu.edu.sg).

Yue Wu, Xipei Yu, and Xiaohua Wang are with the School of Electrical Engineering, Xi'an Jiaotong University, Xi'an 710049, China (e-mail: dywuyue@stu.xjtu.edu.cn; yxp19990719@stu.xjtu.edu.cn; xhw@mail.xjtu.edu.cn).

Ning Wang is with the Department of Energy Technology, Aalborg University, 9220 Aalborg, Denmark (e-mail: nwa@et.aau.dk).

Color versions of one or more figures in this article are available at https://doi.org/10.1109/TPEL.2025.3573737.

Digital Object Identifier 10.1109/TPEL.2025.3573737

I. Introduction

WIRELESS power transfer (WPT) technology has emerged as a groundbreaking solution for efficiently transmitting electrical energy without physical connectors, opening doors to new possibilities across various fields. From medical implants [1], [2], to consumer electronics [3], [4], drones [5], underwater robots [6], [7], industrial automation [8], [9], and electric vehicles [10], [11], [12], ranging from several watts to tens of kilowatts, the widespread applications of WPT technology can significantly improve convenience, enhance user experience, and extend device longevity. Especially since Tesla's high-profile launch of the Robotaxi [13], WPT technology has once again sparked a wave of interest in academic and commercial circles worldwide.

Obviously, it is crucial to reasonably and efficiently design a WPT system for various application scenarios to achieve fast, stable, and safe battery charging with a high transfer efficiency. As the most critical energy conversion module in a WPT system, the resonant network has a decisive impact on the key performance of the WPT system [14]. Before designing a specific resonant network, it is essential to optimize its resonant parameters based on multiple design criteria and requirements.

Many researchers are dedicated to developing practical methods for designing resonant network parameters. Buja et al. [15] took the design of a 500 W wireless charging system for a city car as an example, using a combination of experience and simulation to select the resonant parameters, but without achieving an optimized design. Kim et al. [16] presented a practical design process of resonant parameters of the WPT system by considering multiple factors including current rating, output dc voltage, and transfer power under misalignments. However, they do not provide an intuitive and universal design methodology. In [17], a multiobjective optimization method of a double-D pad for a WPT system is proposed based on the WPT2 defined by SAE J2954 [18]. However, the method for designing coils mentioned above is not universally applicable, as there are only a few specific applications where resonant parameters have established selection standards. In order to meet the constant current (CC) and constant voltage (CV) charging of batteries, Huang et al. [19] are dedicated to developing and

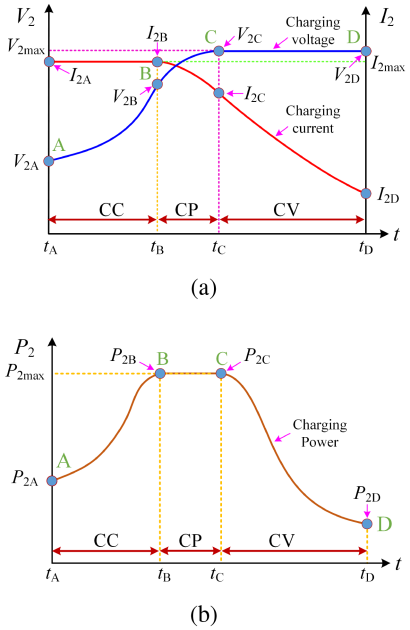

Fig. 1. Charging curves of three-stage charging mode for batteries. (a) Charging voltage V_2 and charging current I_2 versus charging time. (b) Charging power P_2 versus charging time.

deriving a series of WPT systems capable of providing CC and CV output. Unfortunately, the authors cannot provide a resonant network parameter design solution. In summary, there is a lack of a universal method for resonant network parameter design that comprehensively considers multiple factors.

With the continuous development of battery technology, many application demands have an urgent need for shorter charging times, thus requiring WPT technology to enable fast charging. Traditional wireless charging methods for batteries typically employ charging profiles that maintain a CC stage and a CV stage [20], [21], [22]. Since the battery voltage is relatively low at the beginning of CC stage, the charging power starts at a minimum level, slowly rising to its peak near the end of the CC stage, which ultimately results in a slower overall charging rate. Intuitively, applying a higher charging current during the CC charging stage can increase charging rate, but it also places greater demands on thermal management design and accelerates battery aging [23], [24], [25]. Therefore, by incorporating constant power (CP) charging to replace part of the CC stage, the wireless charger can either increase the charging speed with the same setup or reduce overall size and cooling material costs, which eliminates the need for excessive thermal design, as well as mitigates the issue of battery aging.

The typical three-stage charging process for the battery is shown in Fig. 1. In the CC stage, the WPT system first charges the battery with the maximum charging current I_{2max}. As the charging process goes, it will switch from the CC stage to CP stage when the charging power reaches the highest charging power P_{2max}. When the charging voltage V_2 reaches its maximum value V_{2max}, it will switch from the CP stage to the CV stage. In the CV stage, the highest charging voltage V_{2max} is applied to charge the battery until the charging process is completed. Based on the

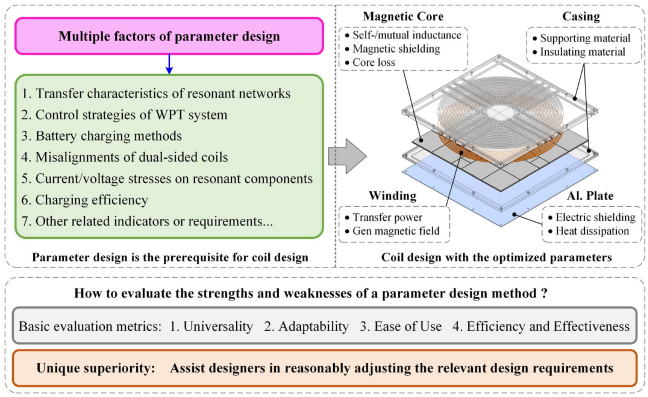

Fig. 2. Design of resonant network parameters and evaluation of design methods.

four special operating points A, B, C, and D shown in Fig. 1, the relationships between the battery voltage, current, power, and equivalent dc resistance at four charging time points are

$$\begin{cases} V_{2A} < V_{2B} < V_{2C} = V_{2D} \\ I_{2A} = I_{2B} > I_{2C} > I_{2D} \\ P_{2A} < P_{2B} = P_{2C} > P_{2D} \\ R_{LA} < R_{LB} < R_{LC} < R_{LD} \end{cases}. \tag{1}$$

With the continuous development of fast charging technology for batteries, the charging power is constantly increasing, which raises higher design requirements for WPT systems. Therefore, it is urgent to develop a universal resonant parameter design method that can adapt to multiscenario applications and achieve fast, stable, safe, economical, and efficient charging. As shown in Fig. 2, when performing the specific design of resonant parameters, an effective parameter design method must take into account multiple factors, including the transfer characteristics of the resonant network, system control strategies, battery charging methods, misalignments of the transmitting (Tx) and receiving (Rx) coils, the voltage and current stresses on resonant components, charging efficiency, and other related indicators or requirements. The structural design of resonant coils can only be carried out after obtaining optimized resonant parameters that meet all electrical characteristics. Moreover, when a resonant parameter design method is proposed, how can the quality of this method be evaluated? Fig. 2 presents four basic evaluation metrics that can roughly assess the quality of a parameter design method, which include the following.

1) Universality: it can be effectively used in various applications and conditions.
2) Adaptability: it can be adjusted to different application environments, handling various constraints and objectives.
3) Ease of use: it is simple to operate and provides clear guidance to designers, reducing development time and learning costs.
4) Efficiency and effectiveness: it should be able to quickly generate solutions that meet the design requirements and deliver high performance, stability, and other key metrics.

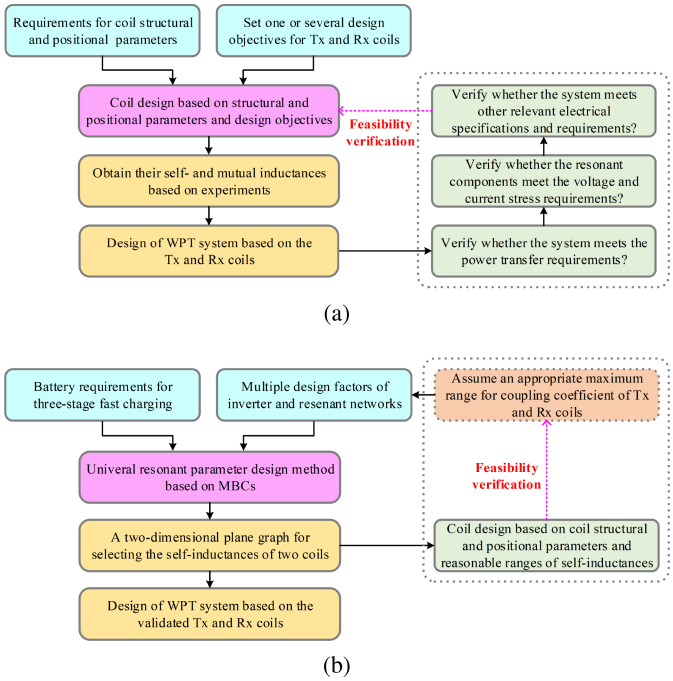

Fig. 3. Comparison of design methods of the WPT system. (a) Traditional design methods based on coil design objectives. (b) Proposed design method based on MBCs.

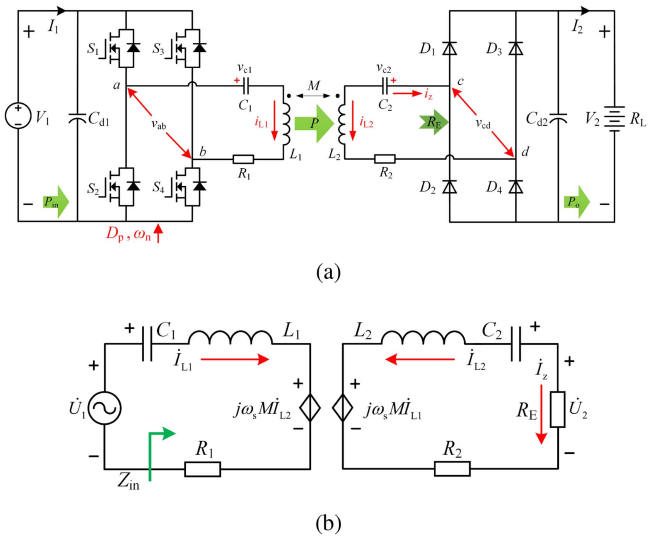

Fig. 4. (a) Schematic of an SS-type WPT system. (b) Its AC equivalent circuit.

In addition to the four basic metrics mentioned above, a more advanced and intelligent design method should be capable of assisting designers in reasonably adjusting the relevant design requirements to optimize the overall performance of the WPT system, which is crucial in practical engineering applications.

To highlight the innovative contribution of this article, Fig. 3 compares the traditional WPT system design method based on coil design objectives with the proposed approach based on multiple boundary constraints (MBCs). As shown in Fig. 3(a), conventional methods usually begin by setting one or more objectives for the Tx and Rx coils, such as quality factor [26], [27], transfer efficiency and power density [28], transfer efficiency, material cost, and misalignment [29], coupling coefficient and leakage flux [17], and so on. Based on the structural and positional constraints, coils are designed and fabricated, which are experimentally measured to obtain their self- and mutual inductances, and subsequently used to construct the WPT system. However, validating whether the system with designed coils meets various performance requirements is a complex and time-consuming process. If any of these requirements are not met, the coils must be redesigned and refabricated, which introduces significant cost and design inefficiencies. Moreover, traditional methods provide limited guidance on how to adjust coil parameters effectively once design issues are identified.

To overcome the shortcomings of the traditional design method of the WPT system that prioritizes coil design objectives, Fig. 3(b) presents a universal resonant parameter design method of the WPT system based on MBCs. Rather than relying solely on predefined coil objectives, this method first assumes a reasonable range for the coupling coefficient based on structural and positional parameters of two coils. It then comprehensively incorporates various design considerations into unified MBCs. Moreover, a 2-D plane graph is introduced to guide the selection of coil self-inductances within the feasible region defined by MBCs. Finally, the coil design is then performed within these boundaries, and feasibility verification is simplified to confirming that the actual coupling falls within the assumed range. Compared to traditional methods, this approach inherently embeds important, complex, and time-consuming validation processes into the design stage with the MBCs and are reflected in the allowable ranges of self-inductance values for the Tx and Rx coils. In addition to producing the optimized coil design, this MBCs-based design method can also assist designers in revising unreasonable indicators, significantly boosting design efficiency, and ensuring the design results completely leverage superior system performance.

The rest of this article is organized as follows. Section II presents the basic analysis of the WPT system and introduces the leap frequency phase shift control (LFPSC) strategy. Section III presents the derivation process of MBCs for optimizing the resonant parameters. Section IV introduces a case-study to detail the process of designing a resonant network using MBCs. Section V validates the design results through simulated and experimental testing. Finally, Section VI concludes this article.

II. Basic Analysis of the WPT System

A. Fundamentals of the WPT System

The schematic of the SS-type WPT system is shown in Fig. 4. Its configuration comprises a high-frequency full-bridge inverter, an SS-type resonant network, and a full-bridge rectifier. The inverter operates in the complementary mode at the frequency ω_s that ranges from tens of kHz to hundreds of kHz. It converts a dc voltage V_1 into a high-frequency ac square voltage v_{ab} that stimulates the primary resonant coil L_1 and resonant

capacitor C_1. Subsequently, the high-frequency alternating magnetic field is generated by L_1, inducing a high-frequency ac voltage in the secondary resonant coil L_2, which powers a load $R_{\rm L}$ with a rectifier.

In general, the fundamental harmonic analysis is commonly applied in the WPT system [30] and its ac equivalent circuit is shown in Fig. 4(b). U_1 and U_2 represent the root mean square (rms) values of fundamental components of $v_{\rm ab}$ and $v_{\rm cd}$, respectively. $I_{\rm L1}$ and $I_{\rm L2}$ represent the rms values of Tx and Rx resonant currents, respectively. R_1 and R_2 denote the equivalent series resistors (ESRs) of the resonant network. L_1 and L_2 represent the self-inductances of Tx and Rx coils, respectively. M is their mutual inductance and their coupling coefficient, k, satisfies

$$k = \frac{M}{\sqrt{L_1 L_2}}. \tag{2}$$

For simplicity, the Tx and Rx resonant frequencies are set to be equal to ω_0 that satisfies

$$\omega_0 = \frac{1}{\sqrt{L_1 C_1}} = \frac{1}{\sqrt{L_2 C_2}}. \tag{3}$$

Therefore, the per-unit value of the operating frequency $\omega_{\rm n}$ can be defined as

$$\omega_{\rm n} = \omega_{\rm s}/\omega_0 \tag{4}$$

where $\omega_{\rm s}$ is the actual operating frequency of the inverter.

B. Characteristics of Resonant Network

To achieve fast and stable charging of the battery, it is essential to fully leverage the transfer characteristics of the resonant network. Based on Fig. 4(b) and (1) in [27], when R_1 and R_2 are neglected, the transconductance gain of the resonant network, $G_{\rm ivss}$, can be obtained by (5) shown at the bottom of this page.

According to (5), $G_{\rm ivss}$ is a function of the ac equivalent load resistance $R_{\rm E}$ and $\omega_{\rm n}$. As shown in Fig. 5(a), when the WPT system operates at point M, it will exhibit CC characteristics regardless of load variations, which is crucial for CC charging of the battery. When $\omega_{\rm n} = 1$, $G_{\rm ivss}$ can be obtained by

$$G_{\rm ivss}(\omega_{\rm n} = 1) = \frac{1}{k\omega_0\sqrt{L_1 L_2}} \tag{6}$$

According to (5), the voltage gain of the resonant network, $G_{\rm vss}$, can also be obtained by (7) shown at the bottom of this page. Similarly, according to (7), $G_{\rm vss}$ is also a function of $R_{\rm E}$ and $\omega_{\rm n}$. When the system operates at point $N_{\rm L}$ or $N_{\rm H}$ in Fig. 5(b),

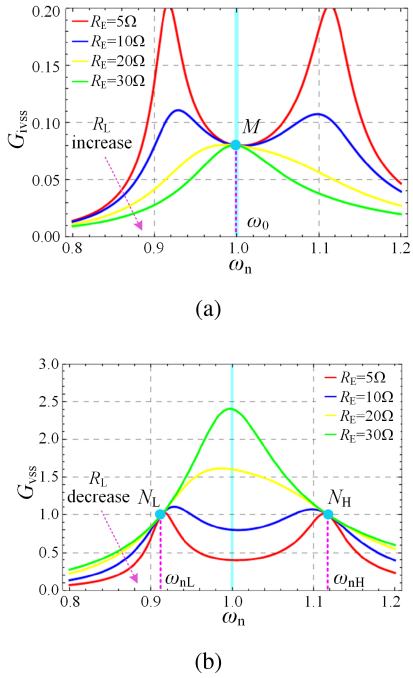

Fig. 5. Transfer characteristics of the ideal SS-type resonant network, $L_1 = L_2 = 116.86$ μH, $C_1 = C_2 = 30$ nF and $k = 0.2$. (a) $G_{\rm ivss}$ versus $\omega_{\rm n}$ with different $R_{\rm E}$. (b) $G_{\rm vss}$ versus $\omega_{\rm n}$ with different $R_{\rm E}$.

it will exhibit CV characteristics regardless of load variations, which is crucial for CV charging of the battery. Based on [31], the operating frequencies at $N_{\rm L}$ and $N_{\rm H}$ are

$$\begin{cases} \omega_{\rm nL} = 1/\sqrt{1+k} & \cdots \text{ Point } N_{\rm L} \\ \omega_{\rm nH} = 1/\sqrt{1-k} & \cdots \text{ Point } N_{\rm H} \end{cases}. \tag{8}$$

Substituting (8) into (7), respectively, it can be obtained that

$$G_{\rm vss}(\omega_{\rm nL}) = G_{\rm vss}(\omega_{\rm nH}) = \sqrt{L_2/L_1}. \tag{9}$$

C. Leap-Frequency Phase Shift Control

To fully utilize the CC/CV characteristics of the resonant network shown in Fig. 5, an LFPSC strategy is adopted to achieve the three-stage fast charging of the battery, which is depicted in Fig. 6. According to the analysis results in Section II-B, when $\omega_{\rm n} = 1$, the WPT system will exhibit CC characteristics regardless of load variations. Correspondingly, when $\omega_{\rm n} = \omega_{\rm nL}$ or $\omega_{\rm nH}$, the WPT system will exhibit CV characteristics regardless of

$$G_{\rm ivss} = \left|\frac{\dot{I}_{\rm z}}{\dot{U}_1}\right| = \frac{kL_2\omega_{\rm n}^3}{\sqrt{L_1 L_2\left(R_{\rm E}^2\omega_{\rm n}^2(\omega_{\rm n}^2-1)^2 + \omega_0^2 L_2^2\left(-1+2\omega_{\rm n}^2+(-1+k^2)\omega_{\rm n}^4\right)^2\right)}} \tag{5}$$

$$G_{\rm vss} = \left|\frac{\dot{U}_2}{\dot{U}_1}\right| = G_{\rm ivss}\times R_{\rm E} = \frac{kL_2\omega_{\rm n}^3 R_{\rm E}}{\sqrt{L_1 L_2\left(R_{\rm E}^2\omega_{\rm n}^2(\omega_{\rm n}^2-1)^2 + \omega_0^2 L_2^2\left(-1+2\omega_{\rm n}^2+(-1+k^2)\omega_{\rm n}^4\right)^2\right)}}. \tag{7}$$

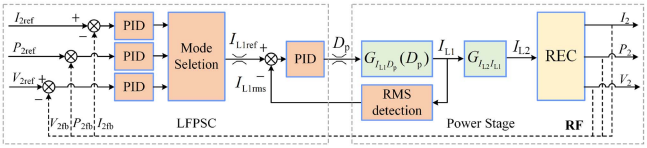

Fig. 6. Flowchart of LFPSC strategy based on the equivalent load resistor.

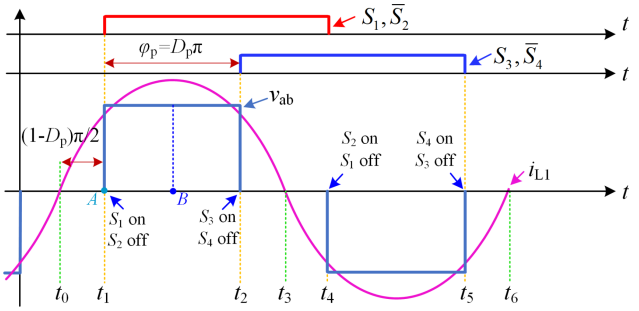

Fig. 7. Operating waveforms of the WPT system with LFPSC in the CC stage.

load variations. Fully utilizing these characteristics can significantly enhance the stability of the WPT system [32].

Based on Fig. 6, the charging process starts by calculating the equivalent dc resistance of the battery R_L based on the secondary controller sampled signals (charging voltage V_2 and current I_2). By comparing the calculated value R_L with the preset critical resistances R_{LB} and R_{LC} in (1), the charging mode will be decided. When the battery is charged at CC stage (or CP stage), the inverter will operate at the constant frequency phase-shift control with $\omega_n = 1$ and set the reference signal of the CC command (or CP command) to I_{2ref} (or P_{2ref}). When the battery operates at the CV stage, the inverter will operate at the constant frequency phase-shift control with $\omega_n = 1/\sqrt{1-k}$ and set the reference signal of the CV command to V_{2ref}.

D. Minimum Phase-Shift Duty Cycle

As shown in Fig. 1(b), the charging power undergoes large variations throughout the entire three-stage charging process. When the LFPSC strategy is adopted in Fig. 6, the control variable phase-shift duty cycle, D_p, will inevitably undergo significant variations. However, a smaller D_p will adversely affect the performance of the WPT system. Take the CC charging stage as an example. To achieve the CC charging characteristic of the SS-type WPT system, the inverter should operate at the resonant frequency. The typical operating waveforms of the WPT system with LFPSC in the CC stage are shown in Fig. 7.

On the one hand, when the inverter operates at Point M in Fig. 5(a) (i.e., $\omega_n = 1$), S_1 and S_2 of the inverter cannot achieve ZVS as long as $D_p < 1$, resulting in a certain level of switching losses. Meanwhile, if i_{L1} remains constant, the switching losses increase as D_p decreases. Therefore, to minimize the switching losses of the inverter as much as possible during the whole charging process, the resonant network parameters should be designed to ensure that D_p does not become too small, thereby

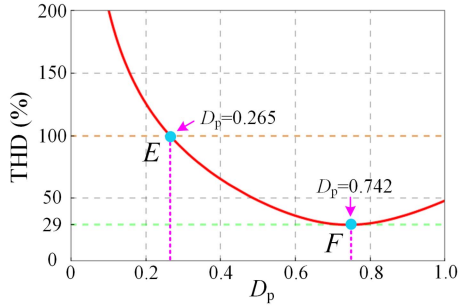

Fig. 8. Relationship between THD and D_p when the LFPSC is applied.

reducing the switching losses of the inverter to the greatest extent possible.

On the other hand, an excessively small D_p tends to introduce a large number of harmonics into the resonant network, thereby increasing the voltage and current stresses on resonant components [33]. In Fig. 7, the fundamental harmonic of the ac square voltage v_{ab}, U_1, can be changed by adjusting the phase-shift duty cycle D_p, which can be calculated by [34]

$$U_1(D_p) = \frac{2\sqrt{2}}{\pi} V_{in} \sin\left[\frac{D_p\pi}{2}\right]. \tag{10}$$

Moreover, based on (10), the total harmonic distortion (THD) of the output ac square voltage of the inverter versus D_p can be calculated by

$$\mathrm{THD}(D_p) = \frac{\sqrt{2\cos[D_p\pi] + 0.5D_p\pi^2 - 2}}{2\sin[0.5D_p\pi]} \times 100\%. \tag{11}$$

Based on (11), the relationship between THD and D_p is plotted in Fig. 8. Obviously, the smaller D_p (lower than 0.742) will lead to the larger THD of the output ac square voltage of the inverter. Therefore, D_p should be larger than a minimum value D_{pmin} in the whole charging process. Notably, assuming the maximum value of THD is set to 1, the corresponding D_{pmin} can be calculated as 0.265.

III. Multiple Boundary Constraints for Resonant Parameter Design

Before designing coils for practical applications, the first step is to determine the self-inductances of Tx and Rx coils. However, it requires a comprehensive consideration of multiple factors, including the transfer characteristics of the resonant network, system control strategies, fast charging (three-stage charging) methods, variations of coupling coefficient, the voltage and current stresses on resonant components, and the limitation of minimum phase-shift duty cycle. Through detailed derivations, these multiple factors can be converted into multiple inequalities that constrain the self-inductances of Tx and Rx coils. The upper and lower limits of these inequalities will define the boundary values for the parameter optimization design of the self-inductances of Tx and Rx coils.

A. Summary of Design Requirements

According to the previous analysis, the design requirements of resonant parameters should satisfy the following.

1) Output Design Requirements: The output design requirements will be discussed in three stages: CC stage, CP stage, and CV stage.

In the CC stage, ω_{n} is set to 1. When $D_{\mathrm{p}}=1$, the output dc current I_2 of the WPT system should be greater than the required maximum charging current $I_{2\mathrm{max}}$. Meanwhile, to limit the minimum D_{p}, I_2 should be less than $I_{2\mathrm{max}}$ when $D_{\mathrm{p}}=D_{\mathrm{pmin}}$. In the CP stage, ω_{n} is set to 1. When $D_{\mathrm{p}}=1$, the output dc power P_2 of the WPT system should be greater than the required maximum charging power $P_{2\mathrm{max}}$. Meanwhile, to limit the minimum D_{p}, P_2 should be less than $P_{2\mathrm{max}}$ when $D_{\mathrm{p}}=D_{\mathrm{pmin}}$. In the CV stage, ω_{n} is set to ω_{nH}. When $D_{\mathrm{p}}=1$, the output dc voltage V_2 of the WPT system should be greater than the required maximum charging voltage $V_{2\mathrm{max}}$. Meanwhile, to limit the minimum D_{p}, V_2 should be less than $V_{2\mathrm{max}}$ when $D_{\mathrm{p}}=D_{\mathrm{pmin}}$. These three aforementioned requirements are collectively referred to as the output design requirements.

2) Current Requirements of Coils: To ensure the safe operation of resonant coils during the whole charging process, the steady-state rms values of resonant coils current on both sides should be less than the preset safety currents I_{L1safe} and I_{L2safe}, respectively.

3) Voltage Requirements of Capacitors: To ensure the safe operation of resonant capacitors during the whole charging process, the steady-state rms values of resonant capacitor voltages on both sides should be less than the preset safety voltages V_{C1safe} and V_{C2safe}, respectively.

B. Boundary Constraints for Output Design Requirements

1) Output Design Requirements in CC Stage: In the CC stage, the equivalent dc resistance of the battery, R_{L}, gradually increases from R_{LA} to R_{LB}. According to (6) and (10), when $\omega_{\mathrm{n}}=1$, the transconductance gain of the system, G_{ivsys}, can be obtained with

$$G_{\mathrm{ivsys}}(\omega_{\mathrm{n}}=1,D_{\mathrm{p}})=\frac{8}{\pi^2\omega_0 k\sqrt{L_1L_2}}\sin\left[\frac{D_{\mathrm{p}}\pi}{2}\right]. \tag{12}$$

Based on (12), it is evident that G_{ivsys} is a monotonically increasing function of D_{p} and a monotonically decreasing function of k. In the CC stage, the desired transconductance gain of the system is defined as $K_{\mathrm{cc}}(=I_{2\mathrm{max}}/V_1)$. Hence, to meet the CC charging requirement when $D_{\mathrm{p}}=1$, G_{ivsys} needs to be not less than K_{cc}, which is

$$G_{\mathrm{ivsys}}(\omega_{\mathrm{n}}=1,D_{\mathrm{p}}=1)\geq K_{\mathrm{cc}}. \tag{13}$$

In addition, an excessively large G_{ivsys} will result in too small D_{p}. Therefore, to limit the minimum D_{p}, when $D_{\mathrm{p}}=D_{\mathrm{pmin}}$, it is required that G_{ivsys} should not exceed K_{cc}, which is

$$G_{\mathrm{ivsys}}(\omega_{\mathrm{n}}=1,D_{\mathrm{p}}=D_{\mathrm{pmin}})\leq K_{\mathrm{cc}}. \tag{14}$$

By substituting (12) into (13) and (14), the self-inductances of Tx and Rx coils in the CC stage should satisfy

$$\frac{64}{\pi^4\omega_0^2k^2K_{\mathrm{cc}}^2L_1}\sin^2\left[\frac{D_{\mathrm{pmin}}\pi}{2}\right]\leq L_2\leq\frac{64}{\pi^4\omega_0^2k^2K_{\mathrm{cc}}^2L_1}. \tag{15}$$

Given that the range of k is $[k_{\mathrm{min}},k_{\mathrm{max}}]$ and denoting the upper and lower limits of L_2 as $L_{2\mathrm{ccu}}$ and $L_{2\mathrm{ccd}}$, respectively, it can be determined that the range of L_2 is

$$\begin{cases}L_{2\mathrm{ccd}} &= \frac{64}{\pi^4\omega_0^2k_{\mathrm{min}}^2K_{\mathrm{cc}}^2L_1}\sin^2\left[\frac{D_{\mathrm{pmin}}\pi}{2}\right]\leq L_2\\ L_{2\mathrm{ccu}} &= \frac{64}{\pi^4\omega_0^2k_{\mathrm{max}}^2K_{\mathrm{cc}}^2L_1}\geq L_2\end{cases}. \tag{16}$$

2) Output Design Requirements in CP Stage: In the CP stage, R_{L} gradually increases from R_{LB} to R_{LC}. Still setting $\omega_{\mathrm{n}}=1$, and based on (12), the output power P_2 is

$$P_2(\omega_{\mathrm{n}}=1,D_{\mathrm{p}})=\frac{64V_1^2R_{\mathrm{L}}}{\pi^4\omega_0^2k^2L_1L_2}\sin^2\left[\frac{D_{\mathrm{p}}\pi}{2}\right]. \tag{17}$$

Similar to CC stage, based on (17), P_2 is also a monotonically increasing function of D_{p} and a monotonically decreasing function of k. By considering both the maximum output power $P_{2\mathrm{max}}$ and the minimum D_{p}, P_2 should satisfy

$$\begin{cases}P_2(\omega_{\mathrm{n}}=1,D_{\mathrm{p}}=1)\geq P_{2\mathrm{max}}\\ P_2(\omega_{\mathrm{n}}=1,D_{\mathrm{p}}=D_{\mathrm{pmin}})\leq P_{2\mathrm{max}}\end{cases}. \tag{18}$$

By substituting (17) into (18), the self-inductances of Tx and Rx coils in the CP stage can be obtained. Moreover, considering that the range of k is $[k_{\mathrm{min}},k_{\mathrm{max}}]$ and the range of R_{L} is $[R_{\mathrm{LB}},R_{\mathrm{LC}}]$, with the upper and lower limits of L_2 denoted as $L_{2\mathrm{cpu}}$ and $L_{2\mathrm{cpd}}$, respectively, L_2 should satisfy

$$\begin{cases}L_{2\mathrm{cpd}} &= \frac{64V_1^2R_{\mathrm{LC}}}{\pi^4\omega_0^2k_{\mathrm{min}}^2L_1P_{2\mathrm{max}}}\sin^2\left[\frac{D_{\mathrm{pmin}}\pi}{2}\right]\leq L_2\\ L_{2\mathrm{cpu}} &= \frac{64V_1^2R_{\mathrm{LB}}}{\pi^4\omega_0^2k_{\mathrm{max}}^2L_1P_{2\mathrm{max}}}\geq L_2\end{cases} \tag{19}$$

By comparing (16) and (19) with the limits set for L_2 in the CC and CP stages, it can be inferred that

$$\begin{cases}L_{2\mathrm{cpu}} &= \frac{64V_1^2R_{\mathrm{LB}}}{\pi^4\omega_0^2k_{\mathrm{max}}^2L_1P_{2\mathrm{max}}}=\frac{64}{\pi^4\omega_0^2k_{\mathrm{max}}^2L_1}\cdot\frac{V_1^2R_{\mathrm{LB}}}{I_{2\mathrm{max}}^2R_{\mathrm{LB}}}=L_{2\mathrm{ccu}}\\ L_{2\mathrm{cpd}} &= \frac{64V_1^2R_{\mathrm{LC}}}{\pi^4\omega_0^2k_{\mathrm{min}}^2L_1P_{2\mathrm{max}}}\sin^2\left[\frac{D_{\mathrm{pmin}}\pi}{2}\right]=\frac{R_{\mathrm{LC}}}{R_{\mathrm{LB}}}L_{2\mathrm{ccd}}>L_{2\mathrm{ccd}}\end{cases}. \tag{20}$$

Then, the range of L_2 constrained in the CC and CP stages is not mutually independent. It is worth mentioning that to make (19) have a solution, it needs to satisfy

$$\sin^2\left[\frac{D_{\mathrm{pmin}}\pi}{2}\right]<\frac{R_{\mathrm{LB}}k_{\mathrm{min}}^2}{R_{\mathrm{LC}}k_{\mathrm{max}}^2}. \tag{21}$$

It is evident that when setting parameter design indicators, these indicators must satisfy (21); otherwise, there will be no solution.

3) Output Design Requirements in CV Stage: In the CV stage, R_{L} increases from R_{LC} to R_{LD}. The resonant network exhibits CV characteristics when $\omega_{\mathrm{n}}=\omega_{\mathrm{nH}}$ or ω_{nL}. Taking into account ZVS characteristics of the inverter, ω_{n} is set to ω_{nH} [35]. According to (9) and (10) with $\omega_{\mathrm{n}}=\omega_{\mathrm{nH}}$, the voltage gain of the

system, G_{vsys}, can be obtained with

$$G_{\text{vsys}}(\omega_{\text{n}}=\omega_{\text{nH}},D_{\text{p}})=G_{\text{ivsys}}\times R_{\text{L}}=\sqrt{\frac{L_2}{L_1}}\sin\left[\frac{D_{\text{p}}\pi}{2}\right]. \tag{22}$$

In the CV stage, the desired voltage gain of the system is defined as $K_{\text{cv}}(=V_{2\max}/V_1)$. By considering both the required K_{cv} and the minimum D_{p}, G_{vsys} should satisfy

$$\begin{cases} G_{\text{vsys}}(\omega_{\text{n}}=\omega_{\text{nH}},D_{\text{p}}=1)\geq K_{\text{cv}} \\ G_{\text{vsys}}(\omega_{\text{n}}=\omega_{\text{nH}},D_{\text{p}}=D_{\text{pmin}})\leq K_{\text{cv}} \end{cases}. \tag{23}$$

By substituting (22) into (23), the self-inductances of Tx and Rx coils in the CV stage should satisfy

$$K_{\text{cv}}^2L_1\leq L_2\leq K_{\text{cv}}^2L_1\csc^2\left[\frac{D_{\text{pmin}}\pi}{2}\right]. \tag{24}$$

Therefore, the range of L_2 in the CV stage is independent of both k and R_{L}.

C. Boundary Constraints for Resonant Coil Currents

Since coil voltages depend on coil currents, once the maximum coil currents are determined, coil voltages can be easily calculated. Therefore, only the constraints on coil currents on both sides are considered here, which should be analyzed separately.

1) Constraints of Secondary Resonant Coil Current: As the secondary side adopts an uncontrolled rectifier, the secondary coil current I_{L2} is only related to the dc output current of the rectifier I_2 and is independent of the operating frequency of the inverter. Then, I_{L2} can be represented as

$$\begin{cases} I_{\text{L2cc}} &= \frac{\pi}{2\sqrt{2}}\times I_{2\max} \quad \text{(a)} \cdots \text{CC stage} \\ I_{\text{L2cp}} &= \frac{\pi}{2\sqrt{2}}\times\sqrt{\frac{P_{2\max}}{R_{\text{L}}}} \quad \text{(b)} \cdots \text{CP stage} \\ I_{\text{L2cv}} &= \frac{\pi}{2\sqrt{2}}\times\frac{V_{2\max}}{R_{\text{L}}} \quad \text{(c)} \cdots \text{CV stage.} \end{cases} \tag{25}$$

In the CC stage, I_{L2cc} is only dependent on $I_{2\max}$ and is independent of R_{L}. In the CP stage, $P_{2\max}$ remains constant and I_{L2cp} decreases as R_{L} increases, reaching its maximum value when $R_{\text{L}}=R_{\text{LB}}$. In the CV stage, $V_{2\max}$ remains constant and I_{L2cv} decreases as R_{L} increases, reaching its maximum value when $R_{\text{L}}=R_{\text{LC}}$.

In summary, during the whole charging process, it is only necessary to consider I_{L2cc} during the CC stage to ensure that the maximum rms value of the secondary coil current does not exceed the preset value I_{L2safe}.

2) Constraints of Primary Resonant Coil Current: The constraints on the primary resonant coil current also need to be discussed separately for each of the three charging stages. According to Fig. 4(b), the primary coil current I_{L1} can be obtained with

$$I_{\text{L1}}(\omega_{\text{n}})=\frac{I_{\text{L2}}\sqrt{64R_{\text{L}}^2\omega_{\text{n}}^2+\pi^4\omega_0^2L_2^2(\omega_{\text{n}}^2-1)^2}}{\pi^2k\sqrt{L_1L_2}\omega_0\omega_{\text{n}}^2}. \tag{26}$$

Substituting (25).(a) into (26) with $\omega_{\text{n}}=1$, the rms value of the primary coil current in the CC stage can be derived as

$$I_{\text{L1cc}}=\frac{2\sqrt{2}I_{2\max}R_{\text{L}}}{\pi k\omega_0\sqrt{L_1L_2}}. \tag{27}$$

Based on (27), during the CC stage, where $I_{2\max}$ remains constant, I_{L1cc} is a monotonically increasing function of R_{L} and a monotonically decreasing function of k. When $R_{\text{L}}=R_{\text{LB}}$ and $k=k_{\min}$, I_{L1cc} reaches its maximum. To ensure the safety of I_{L1cc} during the CC stage, it should be ensured that its maximum rms value does not exceed the predetermined maximum rms value I_{L1safe} (i.e., $I_{\text{L1cc}}\leq I_{\text{L1safe}}$). Then, given that the range of k is $[k_{\min},k_{\max}]$ and the range of R_{L} is $[R_{\text{LA}},R_{\text{LB}}]$, the required self-inductances L_1 and L_2 during the CC stage should satisfy

$$L_2\geq\frac{8I_{2\max}^2R_{\text{LB}}^2}{\pi^2I_{\text{L1safe}}^2k_{\min}^2\omega_0^2L_1}. \tag{28}$$

Substituting (25).(b) into (26) with $\omega_{\text{n}}=1$, the rms value of the primary coil current in the CP stage can also be obtained. Similar to CC stage, to ensure the safety of I_{L1cp} during the CP stage, the required self-inductances L_1 and L_2 should satisfy

$$L_2\geq\frac{8P_{2\max}R_{\text{LC}}}{\pi^2\omega_0^2I_{\text{L1safe}}^2k_{\min}^2L_1} \tag{29}$$

Based on the lower limit constraints for L_2 in the CC and CP stages, by comparing (28) and (29), it can be inferred that

$$\frac{8P_{2\max}R_{\text{LC}}}{\pi^2\omega_0^2I_{\text{L1safe}}^2k_{\min}^2L_1}=\frac{8I_{2\max}^2R_{\text{LC}}R_{\text{LB}}}{\pi^2\omega_0^2I_{\text{L1safe}}^2k_{\min}^2L_1}>\frac{8I_{2\max}^2R_{\text{LB}}^2}{\pi^2\omega_0^2I_{\text{L1safe}}^2k_{\min}^2L_1}. \tag{30}$$

Therefore, according to (30), it is sufficient to focus solely on the lower limit of L_2 in the CP stage. Substituting (25).(c) into (26) with $\omega_{\text{n}}=\omega_{\text{nH}}$, the rms value of the primary coil current in the CV stage can be represented as

$$I_{\text{L1cv}}=\frac{V_{2\max}}{2\sqrt{2}\pi\omega_0}\sqrt{\frac{64(1-k)}{L_1L_2k^2}+\frac{\pi^4\omega_0^2L_2}{R_{\text{L}}^2L_1}}. \tag{31}$$

In the CV stage, where $V_{2\max}$ remains constant, I_{L1cv} is a monotonically decreasing function of both R_{L} and k. Similarly, to ensure the safety of I_{L1cv} during CV stage, the required self-inductances L_1 and L_2 should satisfy

$$L_{2\text{cvd}}^{(1)}\leq L_2\leq L_{2\text{cvu}}^{(1)} \tag{32}$$

where $L_{2\text{cvd}}^{(1)}$ and $L_{2\text{cvu}}^{(1)}$ represent

$$\begin{aligned} L_{2\text{cvd}}^{(1)}&=\frac{4I_{\text{L1safe}}^2L_1R_{\text{LC}}^2}{\pi^2V_{2\max}^2}-\frac{4}{\pi^2}\sqrt{\frac{I_{\text{L1safe}}^4L_1^2R_{\text{LC}}^4}{V_{2\max}^4}-\frac{4(1-k_{\min})R_{\text{LC}}^2}{\omega_0^2k_{\min}^2}} \\ L_{2\text{cvu}}^{(1)}&=\frac{4I_{\text{L1safe}}^2L_1R_{\text{LC}}^2}{\pi^2V_{2\max}^2}+\frac{4}{\pi^2}\sqrt{\frac{I_{\text{L1safe}}^4L_1^2R_{\text{LC}}^4}{V_{2\max}^4}-\frac{4(1-k_{\min})R_{\text{LC}}^2}{\omega_0^2k_{\min}^2}} \end{aligned} \tag{33}$$

In order to ensure that (33) has the solution, the required primary self-inductance L_1 should satisfy

$$L_1\geq\frac{2V_{2\max}^2\sqrt{1-k_{\min}}}{\omega_0k_{\min}I_{\text{L1safe}}^2R_{\text{LC}}}. \tag{34}$$

D. Boundary Conditions for Resonant Capacitor Voltages

Since capacitor currents depends on capacitor voltages, once the maximum capacitor voltages are determined, the capacitor currents can be easily obtained. Therefore, only the constraints on capacitor voltages are required to be considered here, which should also be analyzed separately.

1) Constraints of Secondary Resonant Capacitor Voltage: Based on (25), during three charging stages, the secondary resonant capacitor voltage V_{C2} can be obtained as

$$\begin{cases} V_{C2cc} = \frac{\pi}{2\sqrt{2}} I_{2max}\omega_0 L_2 & (a)\cdots \text{CC stage} \\ V_{C2cp} = \frac{\pi}{2\sqrt{2}}\omega_0 L_2\sqrt{\frac{P_{2max}}{R_L}} & (b)\cdots \text{CP stage} \\ V_{C2cv} = \frac{\pi}{2\sqrt{2}}\frac{V_{2max}\omega_0 L_2\sqrt{1-k}}{R_L} & (c)\cdots \text{CV stage} \end{cases}. \tag{35}$$

Obviously, V_{C2cc} remains constant in the CC stage. In addition, V_{C2cp} reaches its maximum values when $R_L = R_{LB}$ in the CP stage. At point B, V_{C2cc} equals V_{C2cp}. In the CV stage, V_{2max} remains constant and V_{C2cv} decreases as R_L increases, reaching its maximum value when $R_L = R_{LC}$.

Based on (35), during three charging stages, it is required that the rms value of the secondary resonant capacitor voltage V_{C2} does not exceed the predetermined maximum rms value V_{C2safe}. By solving these inequalities, L_2 should satisfy

$$\begin{cases} 0 < L_2 \le \frac{2\sqrt{2}V_{C2safe}}{\pi\omega_0 I_{2max}} = L_{2ua} & (a)\cdots \text{CC stage} \\ 0 < L_2 \le \frac{2\sqrt{2}V_{C2safe}}{\pi\omega_0}\sqrt{\frac{R_{LB}}{P_{2max}}} = L_{2ub} & (b)\cdots \text{CP stage} \\ 0 < L_2 \le \frac{2\sqrt{2}R_{LC}V_{C2safe}}{\pi\omega_0 V_{2max}\sqrt{1-k_{min}}} = L_{2uc} & (c)\cdots \text{CV stage}. \end{cases} \tag{36}$$

According to (36).(a) and (b), in CC and CP stages, $L_{2ua} = L_{2ub}$. Therefore, the constraints of the upper boundaries of L_2 in the CC and CP stages are equivalent. By comparing the constraints of the upper boundaries of L_2 in the CP and CV stages with $R_{LC} > R_{LB}$ and $0 < k_{min} < 1$, it can be obtained that

$$L_{2uc} > \frac{2\sqrt{2}V_{C2safe}}{\pi\omega_0}\sqrt{\frac{R_{LC}}{P_{2max}}} > \frac{2\sqrt{2}V_{C2safe}}{\pi\omega_0}\sqrt{\frac{R_{LB}}{P_{2max}}} = L_{2ub}. \tag{37}$$

According to (37), it can be obtained that $L_{2uc} > L_{2ua} = L_{2ub}$. Therefore, to ensure the safety of V_{C2cv} during CV stage, the secondary self-inductance L_2 should satisfy

$$0 \le L_2 \le \frac{2\sqrt{2}V_{C2safe}}{\pi\omega_0}\sqrt{\frac{R_{LB}}{P_{2max}}}. \tag{38}$$

2) Constraints of Primary Resonant Capacitor Voltage: Similarly, the constraints on the primary resonant capacitor voltage also needs to be discussed separately for each of three charging stages. According to (26), the primary resonant capacitor voltage V_{C1} can be obtained by

$$V_{C1}(\omega_n) = \frac{I_{L2}L_1\sqrt{64R_L^2\omega_n^2 + \pi^4\omega_0^2 L_2^2(\omega_n^2-1)^2}}{\pi^2\omega_n^3 k\sqrt{L_1 L_2}}. \tag{39}$$

In CC and CP stages, substituting (25).(a) and (b) into (39) and $\omega_n = 1$, respectively, V_{C1cc} and V_{C1cp} can be obtained by

$$\begin{cases} V_{C1cc} = \frac{2\sqrt{2}I_{2max}R_L}{\pi k}\sqrt{\frac{L_1}{L_2}} & (a)\cdots \text{CC stage} \\ V_{C1cp} = \frac{2\sqrt{2}}{\pi k}\sqrt{\frac{P_{2max}R_L L_1}{L_2}} & (b)\cdots \text{CP stage} \end{cases}. \tag{40}$$

To ensure the safety of V_{C1cc} and V_{C1cp} during the CC and CP stages, the secondary inductance L_2 should satisfy

$$\begin{cases} L_2 \ge \frac{8L_1 I_{2max}^2 R_{LB}^2}{\pi^2 V_{C1safe}^2 k_{min}^2} & (a)\cdots \text{CC stage} \\ L_2 \ge \frac{8L_1 P_{2max} R_{LC}}{\pi^2 V_{C1safe}^2 k_{min}^2} & (b)\cdots \text{CP stage} \end{cases}. \tag{41}$$

By comparing the lower boundaries of L_2 in (41).(a) and (b), it can be obtained that

$$\frac{8L_1 P_{2max} R_{LC}}{\pi^2 V_{C1safe}^2 k_{min}^2} = \frac{8L_1 I_{2max}^2 R_{LB} R_{LC}}{\pi^2 V_{C1safe}^2 k_{min}^2} > \frac{8L_1 I_{2max}^2 R_{LB}^2}{\pi^2 V_{C1safe}^2 k_{min}^2}. \tag{42}$$

Therefore, based on (42), it's sufficient to focus solely on the lower limit of L_2 in the CP stage. Substituting (25).(c) into (39) and setting $\omega_n = \omega_{nH}$, during CV stage, V_{C1cv} can be derived as

$$V_{C1cv} = \frac{V_{2max}}{2\sqrt{2}\pi}\sqrt{\frac{64L_1}{L_2}\left(\frac{1}{k}-1\right)^2 + \frac{\pi^4\omega_0^2 L_1 L_2(1-k)}{R_L^2}}. \tag{43}$$

As $0 < k < 1$, based on (43), when V_{2max} remains constant, V_{C1cv} is a monotonically decreasing function of R_L and k. Hence, when $R_L = R_{LC}$ and $k = k_{min}$, V_{C1cv} reaches its maximum value. To ensure the safe of V_{C1cv} during CV stage, the required self-inductances L_1 and L_2 should satisfy

$$L_{2cvd}^{(2)} \le L_2 \le L_{2cvu}^{(2)} \tag{44}$$

where $L_{2cvu}^{(2)}$ and $L_{2cvd}^{(2)}$ represent (45). In order to ensure that (45) has the solution, the primary self-inductance L_1 should satisfy

$$L_1 \le \frac{k_{min}R_{LC}V_{C1safe}^2}{2V_{2max}^2\omega_0\sqrt{(1-k_{min})^3}}. \tag{46}$$

E. Summary of Multiple Boundary Constraints

By closely combining transfer characteristics of the resonant network, system control strategies, three-stage charging methods, variations of coupling coefficient, the voltage and current stresses on resonant components and the limitation of minimum phase-shift duty cycle, these upper and lower boundary values of self-inductances of Tx and Rx coils are listed and summarized in Table I. It is worth mentioning that the selected self-inductances of Tx and Rx coils must satisfy all boundary constraints to perform the optimal design of coils, which is named as MBCs.

IV. Case-Study of Coil Design Based on MBCs

To provide a detailed introduction to the proposed universal resonant parameter design method of the WPT system based on MBCs in Fig. 3(b), a detailed explanation will be provided using a specific example in the following.

TABLE I
OPTIMIZED PARAMETER RANGES BASED ON MULTIPLE BOUNDARY CONSTRAINTS

Conditions	No.	Mode	Upper value of L_2	Low value of L_2	Condition
Output Requirements	1	CC	$\frac{64}{\pi^4\omega_0^2 k_{\min}^2 K_{cc}^2 L_1}\sin^2\left[\frac{D_{pmin}\pi}{2}\right]$ *	$\frac{64}{\pi^4\omega_0^2 k_{\max}^2 K_{cc}^2 L_1}$ *	/
	2	CP	$\frac{64V_1^2 R_{LC}}{\pi^4\omega_0^2 k_{\min}^2 L_1 P_{2max}}\sin^2\left[\frac{D_{pmin}\pi}{2}\right]$	$\frac{64V_1^2 R_{LB}}{\pi^4\omega_0^2 k_{\max}^2 L_1 P_{2max}}$	$\sin^2\left[\frac{D_{pmin}\pi}{2}\right] < \frac{R_{LB}k_{\min}^2}{R_{LC}k_{\max}^2}$
	3	CV	$K_{cv}^2 L_1$	$K_{cv}^2 L_1 \csc^2\left[\frac{D_{pmin}\pi}{2}\right]$	/
I_{L1} limitations	4	CC	$\frac{8I_{2max}^2 R_{LB}^2}{\pi^2\omega_0^2 I_{L1safe}^2 k_{\min}^2 L_1}$ *	/	/
	5	CP	$\frac{8P_{2max}R_{LC}}{\pi^2\omega_0^2 I_{L1safe}^2 k_{\min}^2 L_1}$	/	/
	6	CV	$L_{2cvd}^{(1)}$ **	$L_{2cvu}^{(1)}$ **	$L_1 \geq \frac{2V_{2max}^2\sqrt{1-k_{\min}}}{\omega_0 k_{\min} I_{L1safe}^2 R_{LC}}$
V_{C2} limitations	7	CC	/	$\frac{2\sqrt{2}V_{C2safe}}{\pi\omega_0 I_{2max}}$ *	/
	8	CP	/	$\frac{2\sqrt{2}V_{C2safe}}{\pi\omega_0}\sqrt{\frac{R_{LB}}{P_{2max}}}$	/
	9	CV	/	$\frac{2\sqrt{2}R_{LC}V_{C2safe}}{\pi\omega_0 V_{2max}\sqrt{1-k_{\min}}}$ *	/
V_{C1} limitations	10	CC	$\frac{8L_1 I_{2max}^2 R_{LB}^2}{\pi^2 V_{C1safe}^2 k_{\min}^2}$ *	/	/
	11	CP	$\frac{8L_1 P_{2max}R_{LC}}{\pi^2 V_{C1safe}^2 k_{\min}^2}$	/	/
	12	CV	$L_{2cvd}^{(2)}$ **	$L_{2cvu}^{(2)}$ **	$L_1 \leq \frac{k_{\min}R_{LC}V_{C1safe}^2}{2V_{2max}^2\omega_0\sqrt{(1-k_{\min})^3}}$

* Stands for redundant limitations. **The corresponding abbreviations are in (33) and (45).

A. Example of Battery Fast Charging

Based on Fig. 3(b), the example of the battery fast charging by adopting three-stage charging stages will be given first. The target battery pack consists of 12 lead-acid battery modules connected in series, with the nominal capacity and voltage of individual battery modules being 40 A-h and 12 V, respectively. The specific battery parameters are listed in Table II.

B. Design Requirements

In Fig. 3(b), in addition to clarifying the battery parameters in Table II, before designing the resonant parameters, it is also necessary to determine the input dc voltage of the inverter, V_1, the resonant frequency of the resonant network, f_0, the minimum phase-shift duty cycle of the inverter, D_{pmin}, the range of the coupling coefficient, k, the maximum current rms values of Tx and Rx resonant coils for safe operation I_{L1safe} and I_{L2safe}, the maximum voltage rms values of Tx and Rx resonant capacitors for safe operation V_{C1safe} and V_{C2safe}. After determining these specific design specifications, based on Fig. 3(b), the most crucial step is to assume an appropriate maximum range for the coupling coefficient of Tx and Rx coils. The related design specifications are listed in Table III.

C. Optimized Selection Range of Resonant Parameters

Based on Table I, with the related parameters and specifications listed in Tables II and III, the MBCs of self-inductances of Tx and Rx coils are calculated and plotted in Fig. 9(a). Line group ① represents the upper and lower limits of L_2 for satisfying

$$L_{2cvd}^{(2)} = \frac{4R_{LC}^2 V_{C1safe}^2}{\pi^2\omega_0^2(1-k_{\min})V_{2max}^2 L_1} - \frac{4R_{LC}}{\pi^2(1-k_{\min})k_{\min}\omega_0^2}\sqrt{\frac{k_{\min}^2 R_{LC}^2 V_{C1safe}^4}{L_1^2 V_{2max}^4} - 4\omega_0^2(1-k_{\min})^3}$$

$$L_{2cvu}^{(2)} = \frac{4R_{LC}^2 V_{C1safe}^2}{\pi^2\omega_0^2(1-k_{\min})V_{2max}^2 L_1} + \frac{4R_{LC}}{\pi^2(1-k_{\min})k_{\min}\omega_0^2}\sqrt{\frac{k_{\min}^2 R_{LC}^2 V_{C1safe}^4}{L_1^2 V_{2max}^4} - 4\omega_0^2(1-k_{\min})^3} \quad (45)$$

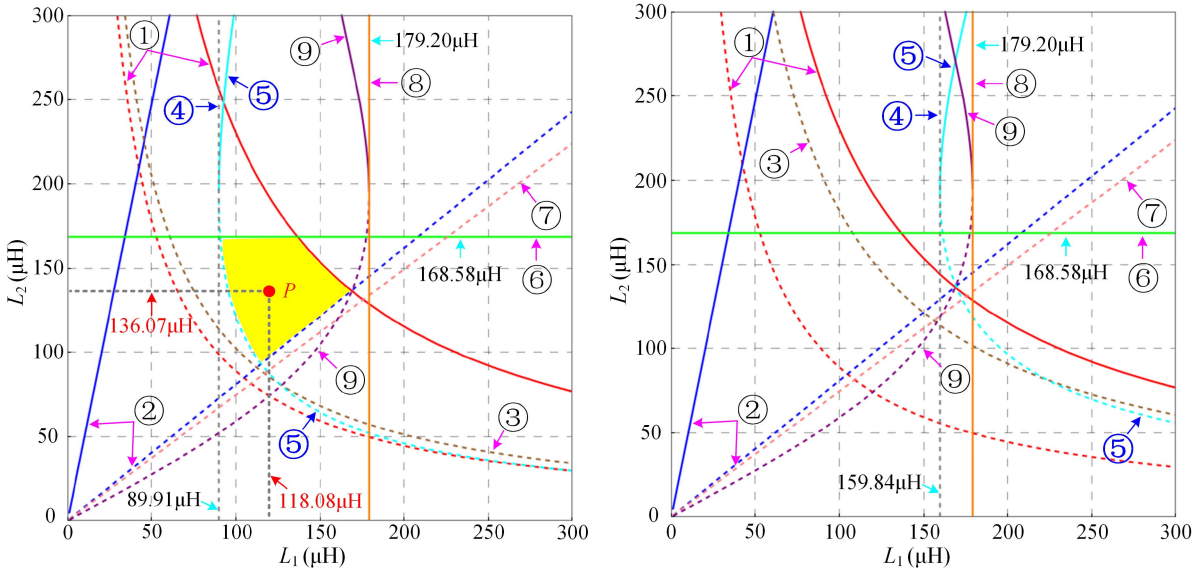

Fig. 9. MBCs of self-inductances of Tx and Rx coils with different I_{L1safe}. (a) MBCs with $I_{\mathrm{L1safe}} = 16$ A. (b) MBCs with $I_{\mathrm{L1safe}} = 12$ A.

TABLE II
BATTERY PARAMETERS WITH THE THREE-STAGE CHARGING

Name	Symbol	Value	Unit
Voltage range of the battery pack modules	V_2	64–144	V
Maximum charging current of the battery pack modules	$I_{2\mathrm{max}}$	8	A
Maximum charging voltage of the battery pack modules	$V_{2\mathrm{max}}$	144	V
Maximum charging power of the battery pack modules	$P_{2\mathrm{max}}$	1000	W
Floating charge current of the battery pack modules	$I_{2\mathrm{min}}$	2	A
Equivalent dc resistance of the battery packs at point A	R_{LA}	8	Ω
Equivalent dc resistance of the battery packs at point B	R_{LB}	15.63	Ω
Equivalent dc resistance of the battery packs at point C	R_{LC}	20.74	Ω
Equivalent dc resistance of the battery packs at point D	R_{LD}	72	Ω

TABLE III
DESIGN SPECIFICATIONS OF INVERTER AND RESONANT NETWORK

Name	Symbol	Value	Unit
DC voltage of inverter	V_2	160	V
Minimum phase-shift duty cycle of inverter	D_{pmin}	0.265	/
Maximum rms value of primary resonant coil current	I_{L1safe}	16	A
Maximum rms value of secondary resonant coil current	I_{L2safe}	12	A
Maximum rms value of primary resonant capacitor voltage	V_{C1safe}	1000	V
Maximum rms value of secondary resonant capacitor voltage	V_{C2safe}	800	V
Maximum range of coupling coefficient	k	0.15–0.20	/
Resonant frequency	f_0	85	kHz

output design requirements in the CP stage (solid line for the upper limit and dashed line for the lower limit). Line group ② represents the upper and lower limits of L_2 for satisfying output design requirements in the CV stage. Line ③ represents the lower limit of L_2 for safe operation of the primary coil in the CP stage. Lines ④ and ⑤ represent the limits of L_1 and L_2 for safe operation of the primary coil in the CV stage. Line ⑥ represents the upper limit of L_2 for safe operation of the secondary resonant capacitor in the CP stage. Line ⑦ represents the lower limit of L_2 for safe operation of the primary resonant capacitor in the CP stage. Lines ⑧ and ⑨ represent the limits of L_1 and L_2 for safe operation of the primary capacitor in the CV stage. Considering all constraints, the optimized range of self-inductances of L_1 and L_2 will be located at the shaded yellow region in Fig. 9(a).

It is worth mentioning that if the shaded region is nonexistent or very small after plotting all boundary constraints, it indicates that the proposed design specifications are unreasonable and need to be re-optimized. Here, if the maximum rms value of primary resonant coil current I_{L1safe} is set as 12 A and the other parameters in Tables II and III remain unchanged, the MBCs of self-inductances of Tx and Rx coils are calculated and plotted in Fig. 9(b). Obviously, in Fig. 9(b), there is no suitable shaded region that allows the WPT system to meet all the predefined specifications. Therefore, to achieve fast charging of the battery in Table II, the design specifications outlined

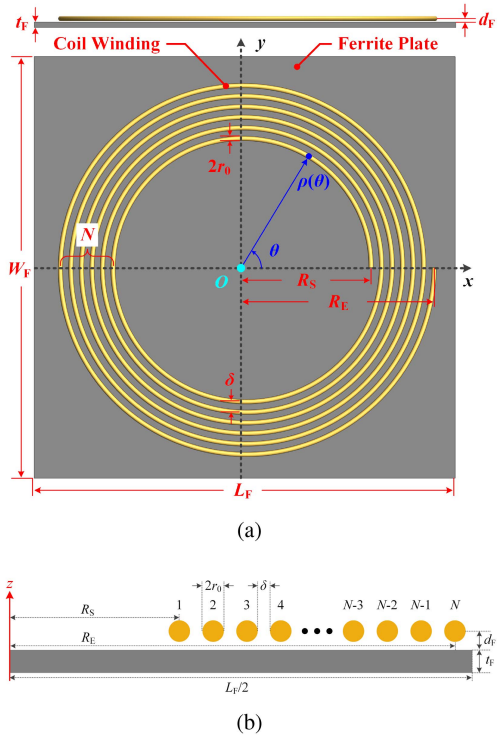

Fig. 10. Structure of the circular coil. (a) Top-down view of the circular coil. (b) Side view of the right half of the circular coil.

in Table III need to be reoptimized to ensure the existence of a valid shaded range of self-inductances for Tx and Rx coils based on MBCs. Generally speaking, the MBCs-based design method of the WPT system not only considers multiple factors to enable the rational design of resonant network parameters but also assists engineers in optimizing design specifications, which significantly accelerates the design process and offers substantial practical value in engineering applications.

D. Coil Design Based on MBCs

Next, we will take the circular coil as an example to detail the MBCs-based design process of Tx and Rx coils.

1) Structure Parameters of a Single Coil: A single circular coil used in this article is shown in Fig. 10. The coil consists mainly of a coil winding and a ferrite plate, whose winding is a planar spiral extending from inside to outside. The radii of the starting and ending points of the coil winding are R_S and R_E, respectively. δ represents the winding pitch, which is the distance between the centers of two adjacent wires. r_0 is the radius of the wire. N_1 and N_2 represent the number of turns of Tx and Rx coils, respectively. W_F, L_F, and t_F represent the width, length, and thickness of the ferrite plate, respectively. d_F is the distance from the center of the wire to the top surface of the ferrite plate. The specific structural parameters are listed in Table IV.

2) Design of Coil Winding Based on MBCs: Before designing the specific coils, it is necessary to determine the transfer distance and misalignment requirements of Tx and Rx coils,

TABLE IV
SPECIFIC STRUCTURAL PARAMETERS OF CIRCULAR COIL

Name	Symbol	Value	Unit
Radius of the starting point of the winding pad	R_S	50	mm
Radius of the ending point of the winding pad	R_E	230	mm
Winding pitch	δ	6	mm
Length of the winding pad	L_{pad}	500	mm
Width of the winding pad	W_{pad}	500	mm
Thickness of the winding pad	t_{pad}	15	mm
Length of the ferrite plate	L_F	450	mm
Width of the ferrite plate	W_F	450	mm
Thickness of the ferrite plate	t_F	5	mm
Distance between the winding and the ferrite plate	d_F	3.1	mm
Radius of the winding	r_0	2.1	mm

TABLE V
TRANSFER DISTANCE AND POSITIONAL MISALIGNMENT REQUIREMENTS

Name	Symbol	Value	Unit
Horizontal misalignment in X/Y direction	dx/dy	+/-50	mm
Horizontal misalignment in Z direction	dz	+/-10	mm
Standard vertical distance	H_{coil}	210	mm

which are decided by practical applications. Table V provides an example of the transfer distance and misalignment requirements for the coil design.

After specifying the structural parameters of Tx and Rx coils in Table IV, the most critical step is to design the number of coil turns, which not only requires the self-inductances of Tx and Rx coils to fall within the shaded closed region in Fig. 9 based on MBCs, but also demands feasibility verification of designed coils under the specific transfer distance and positional misalignments listed in Table V. To obtain better misalignment tolerances, the coils will be designed starting from the outermost turn of the winding pad when the winding pitch is fixed. With the aid of the Ansys Maxwell and the specific structural parameters listed in Table IV, the coil design results are that the number of turns for Tx and Rx coils are $N_1 = 10$ and $N_2 = 11$, respectively, with corresponding self-inductances of 118.08 and 136.07 μH, which is also plotted at point P in Fig. 9(a). The coupling coefficient of Tx and Rx coils obtained from simulation reaches its maximum and minimum values under No. 1 and No. 6 of Table VI, respectively, with values of 0.186 and 0.151. According to the proposed MBCs-based resonant parameter design method of the WPT system in Fig. 3(b), under the preset transfer distance and positional misalignments in Table V, the simulated coupling coefficient range of two coils falls precisely within the previously presumed range of 0.15–0.2. This indicates that the coil design result not only meets the transfer distance and positional misalignment requirements but

TABLE VI
EXPERIMENTAL MEASUREMENT RESULTS OF THE DESIGNED COILS

No.	dx(mm)	dz(mm)	$L_1(\mu$H)	$L_2(\mu$H)	$M(\mu$H)	k
1	0	−10	117.39	135.94	23.11	0.183
2	50	−10	117.53	135.95	21.91	0.173
3	0	0	117.38	135.65	20.99	0.166
4	50	0	117.28	135.71	20.32	0.161
5	0	10	117.15	135.44	19.73	0.157
6	50	10	117.21	135.46	19.07	0.151

also satisfies multiple design factors based on MBCs. Therefore, the coil design result represents an optimized and well-balanced solution with excellent overall performance.

V. EXPERIMENTAL EVALUATION

A. Experimental Prototype

1) Testing of Tx and Rx Circular Coils: Based on the previous analysis in Section IV-D, the designed circular coils with ferrite plates are shown in Fig. 11. They are tested by Impedance Analyzer (HIOKI IM3590) under different misalignments. The experimental measurement results of Tx and Rx coils are shown in Table VI. The comparison results between the simulated results with Ansys Maxwell and the experimental results are plotted in Fig. 12. As shown in Fig. 12(a), the simulated and experimental results for the self-inductances of Tx and Rx coils match well, with a maximum error of less than 1μH between them. Meanwhile, Fig. 12(b) presents the simulated and experimental results for the mutual inductances of Tx and Rx coils also agree well under different misalignment conditions, with a maximum error of less than 1μH between them. The comparison results effectively demonstrate that the constructed coils fully meet the expected design results.

2) Experimental Prototype of the WPT System: To verify the previous analysis, a 1-kW experimental prototype is built up, which is shown in Fig. 13. The prototype includes a dc source (IT6536D), a high-frequency inverter, an SS resonant network, a full-bridge diode rectifier, and an electronic load (IT6006 C). Electrical energy is transferred from the dc source to the electronic load. The primary inverter and secondary rectifier are controlled by two control boards based on DSP283377, respectively. The MOSFETs used in the inverter and the rectifier are IXTQ88N30Ps. Tx and Rx controllers exchange information by the wireless communication modules (RF 2.4 GHz). The coupled coils are made by the Litz wire that is composed of 1000 strands of fine wires, each with a diameter of 0.1 mm. The waveforms are recorded by the oscilloscope (LECROY HD08058) and the overall system efficiency is measured by the power analyzer (WT5000). Detailed experimental parameters are listed in Table VII.

B. Verification of Parameter Design With MBCs

The coils designed with the MBCs-based design method require further validation and discussion regarding key design

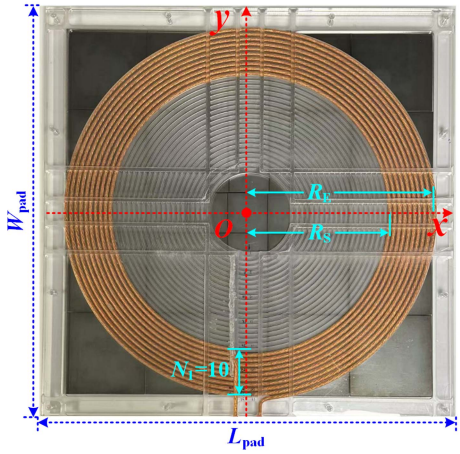

(a)

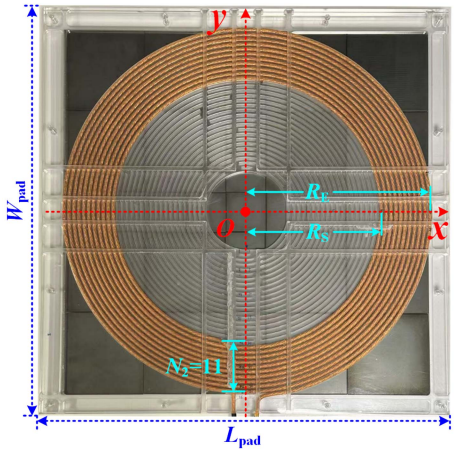

(b)

Fig. 11. Designed winding pads of Tx and Rx circular coils. (a) $N_1 = 10$ for the primary circular coil. (b) $N_2 = 11$ for the secondary circular coil.

TABLE VII
PARAMETERS OF THE WPT SYSTEM

Symbol	Quantity	Value
L_1	primary resonant inductor	117.32 μH
C_1	primary resonant capacitor	29.88 nF
f_1	primary resonant frequency	85 kHz
R_1	primary ESR of resonant network	0.104 Ω
L_2	secondary resonant inductor	135.69 μH
C_2	secondary resonant capacitor	25.40 nF
f_2	secondary resonant frequency	85.73 kHz
R_2	secondary ESR of resonant network	0.119 Ω
R_{dson}	on-time drain-to-source resistance of IXTO88S30Ps	0.04 Ω
R_{L}	load resistor	8 Ω–72 Ω
d	face to face distance of coils	200–220 mm
dx/dy	misalignment in the X/Y direction	+/-50 mm
k	coupling coefficient	0.183–0.151

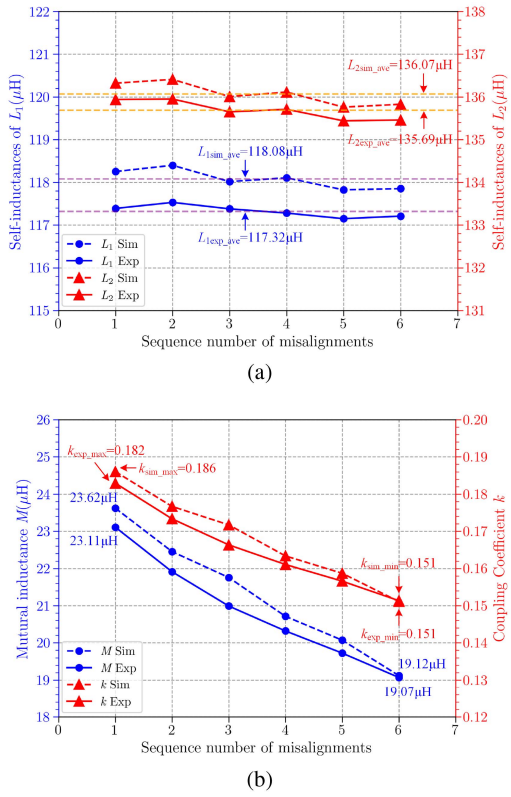

Fig. 12. Comparison of coil parameters between the simulated results and the measured ones. (a) Self-inductances of L_1 and L_2. (b) Mutual inductance and coupling coefficient of L_1 and L_2.

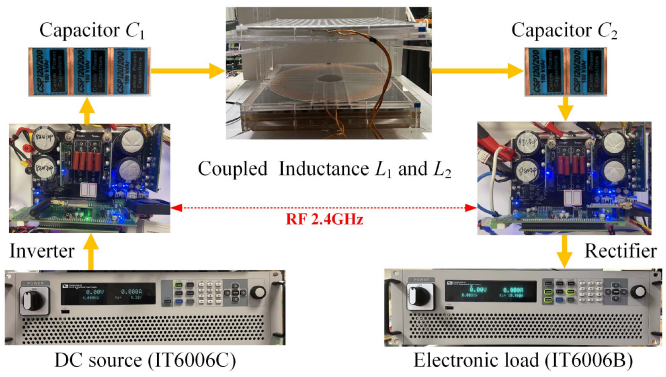

Fig. 13. Experimental prototype.

metrics and outcomes. These primarily include the resonant currents of Tx and Rx coils, the voltages of resonant capacitors on both sides, and the minimum phase-shift duty cycle of the inverter in the whole charging process. Here, the entire battery charging process is simulated by adjusting the load resistor.

1) Verification of Minimum Phase-Shift Duty Cycle: Based on our previous analysis, a smaller phase-shift duty cycle D_p will not only result in higher switching losses of the inverter but also lead to greater THD. Therefore, it is essential to strictly limit the minimum value of D_p throughout the entire battery charging process. When R_L changes, Fig. 14 shows the comparisons between theoretical calculations and simulation

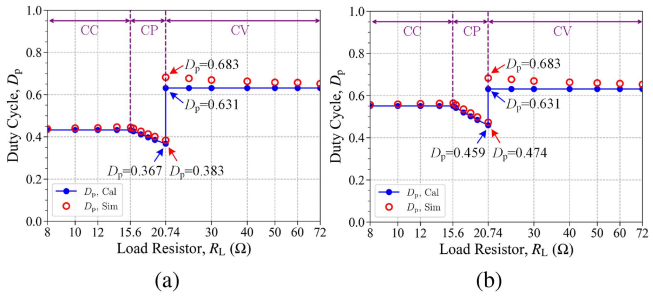

Fig. 14. Comparison of the calculated values with the simulated ones for D_p versus R_L in the three-stage charging process. (a) $k = 0.151$. (b) $k = 0.183$.

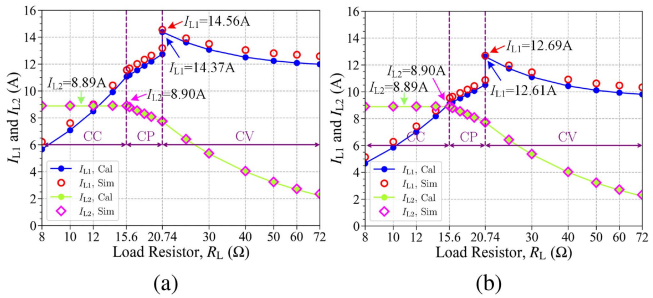

Fig. 15. Comparison of the calculated values with the simulated ones for $I_{\mathrm{L}1}$ and $I_{\mathrm{L}2}$ versus R_L in the three-stage charging process. (a) $k = 0.151$. (b) $k = 0.183$.

measurements of D_p under different k during steady-state operation. The simulated D_p aligns well with the calculated one and the maximum difference between them is 8.24%, which validates the correctness of the theoretical derivation above.

In Fig. 14, during the CC and CV stages, D_p remains almost constant regardless of variations in R_L. It is precisely because the control method and parameter design take into account the CC and CV characteristics of the resonant network that D_p remains almost unchanged with variations of R_L during the CC and CV stages, which greatly reduces the difficulty of designing the closed-loop controller and enhances the stability of the WPT system. In the CP stage, taking into account both coil misalignments and the minimum D_p restriction, the calculated D_p equals 0.367 with $k = 0.151$, which fully meets the previous design requirements ($D_{\mathrm{pmin}} = 0.265$) in the charging process. This proves the effectiveness of the MBCs-based design method.

2) Verification of Resonant Coil Currents: By comparing the calculated results with the simulated results of $I_{\mathrm{L}1}$ and $I_{\mathrm{L}2}$ versus R_L in Fig. 15, the accuracy of the theoretical analysis can be validated. It can be obtained from Fig. 15 that in CC and CP stages of battery charging, $I_{\mathrm{L}1}$ will gradually increase as R_L increases. In the CV stage, $I_{\mathrm{L}1}$ will decrease when R_L increases. When the CP stage turns into the CV stage, $I_{\mathrm{L}1}$ will increase suddenly due to the saltation of the inverter frequency. Obviously, when $R_\mathrm{L} = R_{\mathrm{LC}}$ and $\omega_\mathrm{n} = \omega_{\mathrm{nH}}$, both the calculated results and simulated results of $I_{\mathrm{L}1}$ will reach their maximum values. Therefore, it is precisely due to the insertion of the CP charging stage that, while ensuring a 1 kW charging power, the rms value of $I_{\mathrm{L}1}$ will be greatly reduced. This ensures the safe

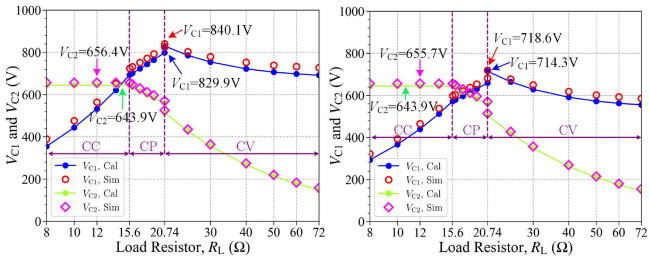

Fig. 16. Comparison of the calculated values with the simulated ones for V_{C1} and V_{C2} versus R_L in the three - stage charging process. (a) $k = 0.151$. (b) $k = 0.183$.

and stable operation of the WPT system without the need for overdesign.

In addition, during the charging process, I_{L2} will reach its maximum value in the CC stage of battery charging, and then gradually decrease as R_L increases. The maximum values of the calculated results and simulated results of I_{L1} and I_{L2} are all below the preset maximum rms values of resonant currents of Tx and Rx coils, respectively, which proves the effectiveness of the MBCs-based design method.

3) Verification of Resonant Capacitor Voltages: By comparing the calculated results with the simulated results of V_{C1} and V_{C2} versus R_L in Fig. 16, the accuracy of the theoretical analysis can also be validated. During the charging process, the variation trends of the resonant capacitor voltages are completely consistent with that of the resonant coil currents. It is worth mentioning that, due to the insertion of the CP charging stage, the rms value of V_{C1} is reduced, which eliminates the need for overdesign of the capacitor voltage. The maximum values of the calculated and simulated results of V_{C1} and V_{C2} are lower than the preset maximum values of resonant voltage V_{C1safe} for the primary capacitor and V_{C2safe} for the secondary capacitor, respectively, which also proves the effectiveness of the MBCs design method.

C. Performance Testing of the WPT System

In order to further verify the rationality of the coil design using the MBCs-based method, it is necessary to test the steady-state and dynamic performance of the WPT system throughout the entire charging process.

1) Testing of Steady-State Performance: The different charging stages of the battery are simulated by changing R_L. Fig. 17 presents the steady-state operating waveforms of the WPT system at different charging stages under the worst operating conditions ($H_{coil} = 220$ mm and d$x = 50$ mm). According to Fig. 17(a) and (b), when the WPT system operates in the CC and CP stages, the operating frequency is fixed at 85 kHz, which enables the WPT system to achieve CC characteristics unaffected by load variations, contributing to improved system stability. In addition, during the CV stage, the operating frequency is switched from 85 to 92.25 kHz, enabling the system to achieve CV characteristics unaffected by load variations under the worst operating conditions, which also contributes to improved system stability.

According to experimental results, throughout the full-range charging process of the battery, the predefined multiple design specifications, including phase-shift duty cycle, resonant coil currents, and resonant capacitor voltages, can all be satisfied under worst operating conditions. Therefore, it effectively demonstrates the validity of the proposed universal resonant parameter design method of the WPT system based on MBCs.

2) Testing of Dynamic Performance: As shown in Fig. 18, the dynamic performance of the WPT system against load disturbances at different charging stages is tested by introducing the step changes of the load resistor R_L.

Fig. 18(a) shows the dynamic responses of the WPT system in the CC stage, where I_2 remains constant at 8 A while R_L is abruptly changed from 8 to 12 Ω. The dynamic setting time is 125 ms. More effectively, Fig. 18(b) presents the dynamic responses of the WPT system in the CP stage, where P_2 remains constant at 1kW while R_L is abruptly changed from 16 to 20 Ω. The dynamic setting time is 17.8 ms. Even more surprisingly, Fig. 18(c) presents the dynamic responses of the WPT system in the CV stage, where V_2 remains constant at 144 V while R_L is abruptly changed from 25 to 40 Ω. The dynamic setting time is only 1.9 ms.

Although this article does not model the entire control system or optimize the controller design, the WPT system still demonstrates excellent dynamic response and antidisturbance performance, which is attributed to the careful consideration of its transfer characteristics when optimizing the design of the resonant network parameters. From this perspective, the coil optimization design method based on MBCs is also of significant importance for improving the system's dynamic response characteristics.

D. Comparison with Other Design Solutions

To further demonstrate the overall superior performance of our design, two other design results are selected as control groups for a comprehensive performance comparison. For a fair comparison, when selecting the coil design solutions for the control groups, we refer to the MBCs design results in Fig. 9(a) and choose two sets of coil design solutions that are close to the shaded region but not within it. The corresponding simulation models are then built in Fig. 19. Except for the difference in the number of coil turns, all other coil structural and positional parameters follow those listed in Tables IV and V. The coil parameters and simulated results for these three cases are listed in Table VIII.

These three solutions of coils are applied to implement the three-stage battery charging. Through MATLAB simulation, key design metrics are compared, including the resonant currents of Tx and Rx coils, the voltages of resonant capacitors on both sides, and the minimum phase-shift duty cycle of the inverter in the whole charging process. As shown in Fig. 20, two radar charts are applied to compare the key design specifications of the WPT system under different coil positions with three different coil design solutions.

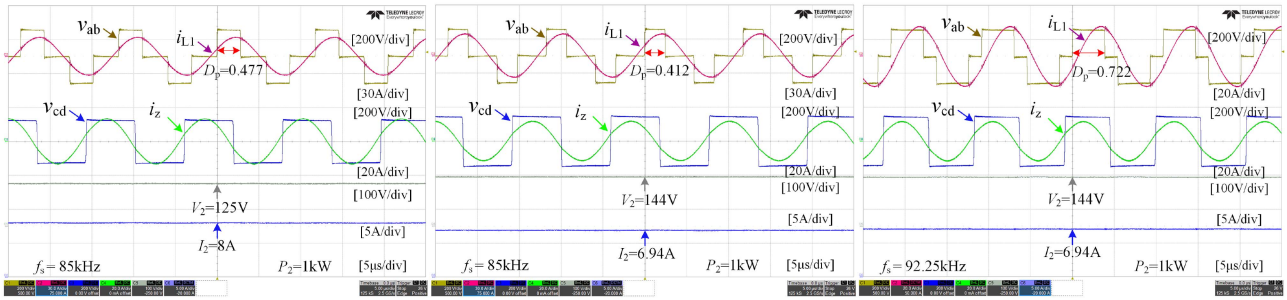

Fig. 17. Steady-state operating waveforms of the WPT system with the optimized coils under $k = 0.151$ and $V_1 = 160\,\text{V}$. (a) In the CC stage, $I_2 = 8\,\text{A}$ and $R_\text{L} = 15.63\,\Omega$. (b) In the CP stage, $P_2 = 1\,\text{kW}$ and $R_\text{L} = 20.74\,\Omega$. (c) In the CV stage, $V_2 = 144\,\text{V}$ and $R_\text{L} = 20.74\,\Omega$.

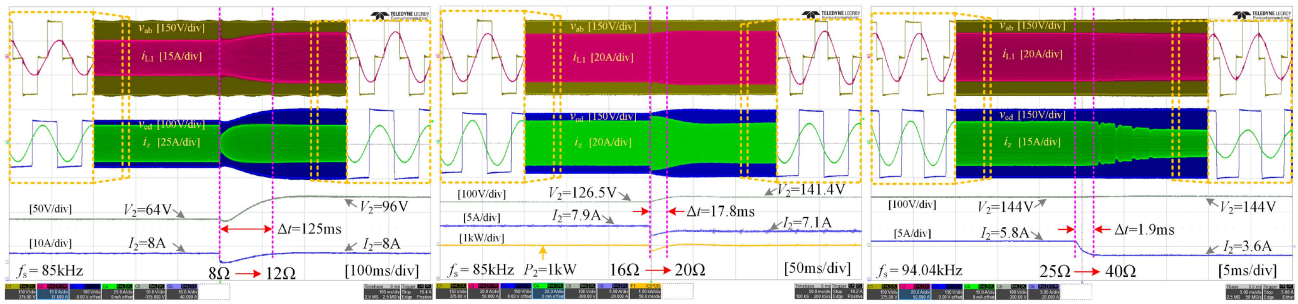

Fig. 18. Dynamic operating waveforms of the WPT system with the optimized coils under $k = 0.183$ and $V_1 = 160\,\text{V}$. (a) In the CC stage, $I_2 = 8\,\text{A}$ and the step change of R_L from 8 to 12 Ω. (b) In the CP stage, $P_2 = 1\,\text{kW}$ and the step change of R_L from 16 to 20 Ω. (c) In the CV stage, $V_2 = 144\,\text{V}$ and the step change of R_L from 25 to 40 Ω.

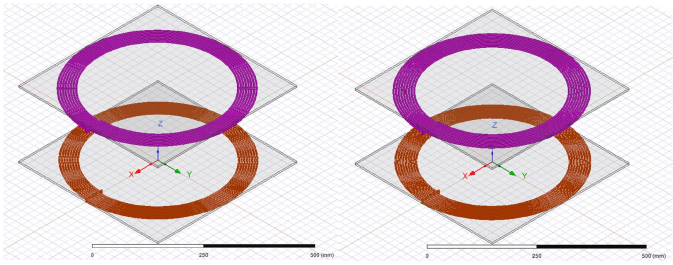

Fig. 19. Two other design solutions for comparison with different numbers of coil turns for Tx and Rx coils. (a) Control Group A, $N_1 = N_2 = 8$. (b) Control Group B, $N_1 = N_2 = 9$.

TABLE VIII
COIL PARAMETERS FOR THREE CASES

Symbol	Control Group A (C. G. A)	Control Group B (C. G. B)	Optimal design in our particle
N_1	8	9	10
N_2	8	9	11
L_1 (μH)	83.69	100.60	118.08
L_2 (μH)	83.68	100.60	136.07
k_min	0.143	0.147	0.151
k_max	0.175	0.180	0.183

In Fig. 20, the regular pentagon formed by the orange dashed line represents the predefined design specifications of the WPT system in Table III. Since the phase-shift duty cycle D_p is expected to be greater than the preset D_pmin and a larger D_p actually corresponds to lower switching losses, the constraint on D_p is represented by the magnitude of the $1 - D_\text{p}$ axis in the radar chart. Based on Fig. 20, it can be observed that only the optimal design in this study ensures that all key design indicators meet the predefined specifications in Table III. Compared with Control Group A and Control Group B, under the same transfer distance and misalignments while delivering the same power, despite the slight increase of V_C2 caused by the tuning of the secondary resonant parameters, the optimal design in this study will exhibit lower I_L1, lower V_C1, larger D_p, lower inverter switching losses, and lower THD in the resonant network. This strongly demonstrates that the proposed universal resonant parameter design method of the WPT system based on MBCs can effectively provide an optimized and well-balanced solution for the WPT system with excellent overall performance.

E. System Transfer Efficiency

With the help of LFPSC strategy, the system charging power and transfer efficiency versus R_L under different misalignments are shown in Fig. 21. Here, the ever-changing R_L is applied to simulate the steady-state fast charging process.

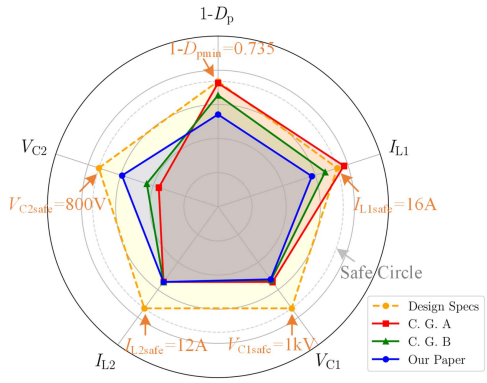

(a)

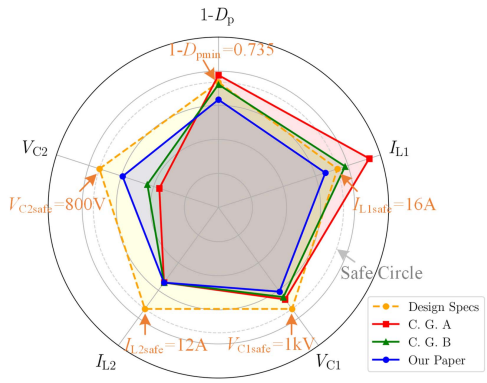

(b)

Fig. 20. Radar comparison charts of key design indicators for three different design solutions of Tx and Rx coils. (a) $\mathrm{d}x = \mathrm{d}y = 0$ mm and $H_{\mathrm{coil}} = 200$ mm. (b) $\mathrm{d}x = 50$ mm, $\mathrm{d}y = 0$ mm, and $H_{\mathrm{coil}} = 220$ mm.

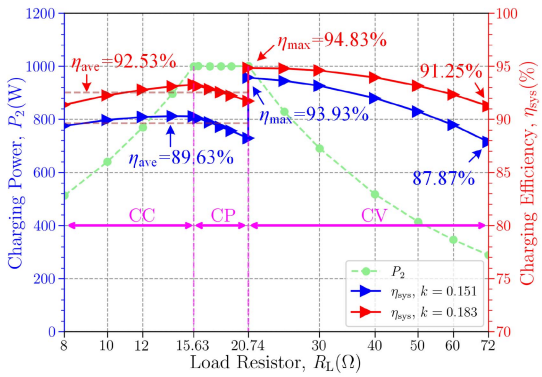

Fig. 21. Charging power and charging efficiency in the three-stage charging process.

In the CC stage, as R_{L} gradually increases, the dc–dc transfer efficiency of the WPT system gradually increases. The exact opposite occurs in the CP stage, where the transfer efficiency gradually decreases as R_{L} increases. In summary, during these two charging stages, the overall average transfer efficiency of the WPT system can achieve 92.53% at $k = 0.183$ as well as 89.63% at $k = 0.151$. However, when the WPT system switches from CP charging to CV charging, the dc–dc transfer efficiency of the system experiences a significant increase. This is because when the system operates at a high-frequency CV gain point [ω_{nH} in Fig. 5(b)], all switching devices of the inverter can achieve ZVS. Generally speaking, with a coupling coefficient k of 0.183 or 0.151, the maximum dc–dc system efficiency reaches 94.83% or 93.93%, respectively, under the rated-load condition (i.e., 1 kW). Notably, when the WPT system operates at point D (i.e., 28.8% of 1 kW), the system efficiency remains as high as 91.25% or 87.87%, respectively.

Generally speaking, the experimental results demonstrate that the well-designed WPT system with the universal resonant parameter design method based on MBCs not only achieves the multiple design targets mentioned before but also achieves high transfer efficiency throughout the full range of battery charging. Therefore, the MBCs-based design method of the WPT system exhibits an optimized and well-balanced solution with excellent overall performance, which is of great significance for practical engineering applications.

VI. Conclusion

This article takes the SS-type WPT system for fast battery charging as an example and proposes a universal resonant parameter design method of the WPT system based on MBCs. This method innovatively transforms all design considerations into constraint relationships and utilizes a 2-D plane graph to optimize self-inductances of Tx and Rx coils. The proposed MBCs-based parameter design method not only exhibits the optimal design of self-inductances for Tx and Rx coils but also assists designers in revising unreasonable design indicators, significantly boosting design efficiency and ensuring the design results completely leverage superior system performance. Experimental results demonstrate that the resonant coils with the MBCs-based design method enable the WPT system to meet all predefined specifications while achieving steady-state and dynamic performance, accompanied by satisfactory dc–dc charging efficiency. Therefore, this design method allows the designed WPT system to achieve fast, stable, and safe battery charging at lower costs and higher charging efficiency, which is crucial for practical applications.

References

[1] S. Roy, A. N. M. W. Azad, S. Baidya, M. K. Alam, and F. Khan, "Powering solutions for biomedical sensors and implants inside the human body: A comprehensive review on energy harvesting units, energy storage, and wireless power transfer techniques," *IEEE Trans. Power Electron.*, vol. 37, no. 10, pp. 12237–12263, Oct. 2022.

[2] R. Sedehi et al., "A wireless power method for deeply implanted biomedical devices via capacitively coupled conductive power transfer," *IEEE Trans. Power Electron.*, vol. 36, no. 2, pp. 1870–1882, Feb. 2021.

[3] A. D. de Sousa, L. F. M. Vieira, and M. A. M. Vieira, "Optimal transmission range and charging time for Qi-compliant systems," *IEEE Trans. Power Electron.*, vol. 35, no. 12, pp. 12765–12772, Dec. 2020.

[4] J. Zhu, Y. Ban, R. Xu, and C. C. Mi, "An NFC-Connected coupler using IPT-CPT-combined wireless charging for metal-cover smartphone applications," *IEEE Trans. Power Electron.*, vol. 36, no. 6, pp. 6323–6338, Jun. 2021.

[5] M. Liao et al., "UAV fleet charging on telecom towers with differential capacitive wireless power transfer," *IEEE Trans. Power Electron.*, vol. 40, no. 4, pp. 6370–6384, Apr. 2025.

[6] D. Wang, F. Chen, J. Zhang, S. Cui, Z. Bie, and C. Zhu, "A novel pendulum-type magnetic coupler with high misalignment tolerance for AUV underwater wireless power transfer systems," *IEEE Trans. Power Electron.*, vol. 38, no. 12, pp. 14861–14871, Dec. 2023.
[7] K. Zhang, Y. Ma, Z. Yan, Z. Di, B. Song, and A. P. Hu, "Eddy current loss and detuning effect of seawater on wireless power transfer," *IEEE J. Emerg. Sel. Topics Power Electron.*, vol. 8, no. 1, pp. 909–917, Mar. 2020.
[8] L. J. Chen, J. T. Boys, and G. A. Covic, "Power management for multiple-pickup IPT systems in materials handling applications," *IEEE J. Emerg. Sel. Topics Power Electron.*, vol. 3, no. 1, pp. 163–176, Mar. 2015.
[9] C. Jiang, K. T. Chau, C. Liu, and W. Han, "Design and analysis of wireless switched reluctance motor drives," *IEEE Trans. Ind. Electron.*, vol. 66, no. 1, pp. 245–254, Jan. 2019.
[10] Y. Li, S. Wang, Y. Wu, Y. Jiang, Z. Xiao, and Y. Tang, "Heterogeneous integration of isotropic and anisotropic magnetic cores for inductive power transfer," *IEEE Trans. Power Electron.*, vol. 40, no. 2, pp. 3770–3784, Feb. 2025.
[11] M. Wu et al., "A compact coupler with integrated multiple decoupled coils for wireless power transfer system and its anti-misalignment control," *IEEE Trans. Power Electron.*, vol. 37, no. 10, pp. 12814–12827, Oct. 2022.
[12] M. Wu et al., "A dual-sided control strategy based on mode switching for efficiency optimization in wireless power transfer system," *IEEE Trans. Power Electron.*, vol. 36, no. 8, pp. 8835–8848, Aug. 2021.
[13] I. Tesla, "We, robot," 2024. [Online]. Available: https://www.tesla.com/we-robot
[14] Y. Wu, Y. Jiang, Y. Li, H. Yuan, X. Wang, and Y. Tang, "Precise parameterized modeling of coil inductance in wireless power transfer systems," *IEEE Trans. Power Electron.*, vol. 39, no. 9, pp. 11746–11757, Sep. 2024.
[15] G. Buja, M. Bertoluzzo, and K. N. Mude, "Design and experimentation of WPT charger for electric city car," *IEEE Trans. Ind. Electron.*, vol. 62, no. 12, pp. 7436–7447, Dec. 2015.
[16] M. Kim, H. Park, and J. Jung, "Practical design methodology of IH and IPT dual-functional apparatus," *IEEE Trans. Power Electron.*, vol. 35, no. 9, pp. 8897–8901, Sep. 2020.
[17] Z. Luo, X. Wei, M. G. S. Pearce, and G. A. Covic, "Multiobjective optimization of inductive power transfer double-D pads for electric vehicles," *IEEE Trans. Power Electron.*, vol. 36, no. 5, pp. 5135–5146, May 2021.
[18] SAE J2954, "Wireless power transfer for light-duty plug-in/electric vehicle and alignment methodology," SAE International, Aug. 2024. [Online]. Available: https://www.sae.org/standards/content/j2954_202408/
[19] Z. Huang, T. Qin, X. L. Li, L. Ding, H. H. Iu, and C. K. Tse, "Synthesis of inductive power transfer converters with dual immittance networks for inherent CC-to-CV charging profiles," *IEEE Trans. Power Electron.*, vol. 39, no. 6, pp. 7766–7777, Jun. 2024.
[20] Z. Li, J. He, Y. Huo, M. Ban, Y. Liu, and J. Liu, "High-misalignment tolerance and output adjustable wireless charging system via detuned series–series compensated reconfigurable transmission channels," *IEEE Trans. Power Electron.*, vol. 38, no. 10, pp. 11786–11801, Oct. 2023.
[21] K. Song, Z. Li, J. Jiang, and C. Zhu, "Constant current/voltage charging operation for series–series and series–parallel compensated wireless power transfer systems employing primary-side controller," *IEEE Trans. Power Electron.*, vol. 33, no. 9, pp. 8065–8080, Sep. 2018.
[22] Y. Jiang, L. Wang, J. Fang, R. Li, R. Han, and Y. Wang, "A high-efficiency ZVS wireless power transfer system for electric vehicle charging with variable angle phase shift control," *IEEE J. Emerg. Sel. Topics Power Electron.*, vol. 9, no. 2, pp. 2356–2372, Apr. 2021.
[23] K. Liu, K. Li, Q. Peng, and C. Zhang, "A brief review on key technologies in the battery management system of electric vehicles," *Front. Mech. Eng.*, vol. 14, no. 1, pp. 47–64, 2019.
[24] M. Yilmaz and P. T. Krein, "Review of battery charger topologies, charging power levels, and infrastructure for plug-in electric and hybrid vehicles," *IEEE Trans. Power Electron.*, vol. 28, no. 5, pp. 2151–2169, May 2013.
[25] I. Iam, C. Choi, C. Lam, P. Mak, and R. P. Martins, "A constant-power and optimal-transfer-efficiency wireless inductive power transfer converter for battery charger," *IEEE Trans. Ind. Electron.*, vol. 71, no. 1, pp. 450–461, Jan. 2024.
[26] M. Budhia, G. A. Covic, and J. T. Boys, "Design and optimization of circular magnetic structures for lumped inductive power transfer systems," *IEEE Trans. Power Electron.*, vol. 26, no. 11, pp. 3096–3108, Nov. 2011.
[27] Z. Huang, S. Wong, and C. K. Tse, "Design of a single-stage inductive-power-transfer converter for efficient EV battery charging," *IEEE Trans. Veh. Technol.*, vol. 66, no. 7, pp. 5808–5821, Jul. 2017.
[28] R. Bosshard, J. W. Kolar, J. Muhlethaler, I. Stevanovic, B. Wunsch, and F. Canales, "Modeling and eta-alpha-Pareto optimization of inductive power transfer coils for electric vehicles," *IEEE J. Emerg. Sel. Topics Power Electron.*, vol. 3, no. 1, pp. 50–64, Mar. 2015.
[29] M. Moghaddami, A. Anzalchi, A. Moghadasi, and A. Sarwat, "Pareto optimization of circular power pads for contactless electric vehicle battery charger," in *Proc. IEEE Ind. Appl. Soc. Annu. Meeting*, 2016, pp. 1–6.
[30] H. Li, J. Li, K. Wang, W. Chen, and X. Yang, "A maximum efficiency point tracking control scheme for wireless power transfer systems using magnetic resonant coupling," *IEEE Trans. Power Electron.*, vol. 30, no. 7, pp. 3998–4008, Jul. 2015.
[31] Q. Chen, S. C. Wong, C. K. Tse, and X. Ruan, "Analysis, design, and control of a transcutaneous power regulator for artificial hearts," *IEEE Trans. Biomed. Circuits Syst.*, vol. 3, no. 1, pp. 23–31, Feb. 2009.
[32] W. Zhang, S. Wong, C. K. Tse, and Q. Chen, "Design for efficiency optimization and voltage controllability of series–series compensated inductive power transfer systems," *IEEE Trans. Power Electron.*, vol. 29, no. 1, pp. 191–200, Jan. 2014.
[33] L. Jiang and D. Costinett, "A high-efficiency GaN-based single-stage 6.78 MHz transmitter for wireless power transfer applications," *IEEE Trans. Power Electron.*, vol. 34, no. 8, pp. 7677–7692, Aug. 2019.
[34] Y. Jiang, L. Wang, J. Fang, C. Zhao, K. Wang, and Y. Wang, "A joint control with variable ZVS angles for dynamic efficiency optimization in wireless power transfer system," *IEEE Trans. Power Electron.*, vol. 35, no. 10, pp. 11064–11081, Oct. 2020.
[35] Y. Jiang, L. Wang, Y. Wang, J. Liu, X. Li, and G. Ning, "Analysis, design, and implementation of accurate ZVS angle control for EV battery charging in wireless high-power transfer," *IEEE Trans. Ind. Electron.*, vol. 66, no. 5, pp. 4075–4085, May 2019.

Yongbin Jiang (Member, IEEE) received the B.S. degree in electrical automatization from Jiangsu University, Zhenjiang, China, in 2012, and the M.S. degree in instrument science and technology and the Ph.D. degree in electrical engineering from Xi'an Jiaotong University, Xi'an, China, in 2016 and 2020, respectively.

From 2020 to 2022, he worked as the Director of Digital Energy Laboratory, UNISOC (Shanghai) Technologies Co., Ltd, Shanghai, China. Since 2022, he has been a Research Fellow with Nanyang Technological University, Singapore. His research interests include wireless power transfer, high frequency and high power density dc/dc converters, signal processing, and digital control technology.

Dr. Jiang was the recipient of the Best Paper Award of IEEE 10th International Symposium on Power Electronics for Distributed Generation Systems in 2019 and the Best ECCE Paper on Emerging Technology Award from IEEE PELS in 2020.

Yue Wu (Student Member, IEEE) received the B.S. degree in electrical engineering in 2018 from the School of Electrical Engineering, Xi'an Jiaotong University, Xi'an, China, where he is currently working toward the Ph.D. degree in electrical engineering.

From September 2022 to March 2024, he is working as a jointly supervised Ph.D. student with Nanyang Technological University. His main research interests include wireless power transfer, design, modeling, and optimization of resonant coils.

Yaohua Li (Student Member, IEEE) received the B.Eng. degree in electrical engineering from University of Calgary, Calgary, Canada, in 2020, and the M.Sc. degree in power engineering in 2021 from Nanyang Technological University, Singapore, where he is currently working toward the Ph.D. degree in electrical engineering.

His research interests include wireless power transfer, high-frequency magnetics, and artificial intelligence.

Ning Wang (Student Member, IEEE) received the B.Eng. degree in electrical engineering from Jilin University, Changchun, China, in 2015, and the M.Sc. degree in electrical engineering from Xi'an Jiaotong University, Xi'an, China, in 2018. He is currently working toward the Ph.D. degree in electrical engineering with Aalborg University, Aalborg, Denmark.

His research interests include dc–dc converter, advance control algorithm, and renewable energy system.

Xipei Yu (Student Member, IEEE) received the B.S. degree in electrical engineering from Xi'an Jiaotong University, Xi'an, China, in 2021. He is currently working toward the Ph.D. degree in electrical engineering with the Center for Power Electronics Systems, Virginia Tech, Blacksburg, VA, USA.

His research interests include high frequency power conversion, wireless power transfer, and resonant converters.

Xiaohua Wang (Senior Member, IEEE) received the B.S. degree from Chang'an University, Xi'an, China, in 2000, and the Ph.D. degree from the School of Electrical Engineering, Xi'an Jiaotong University, Xi'an, in 2006, both in electrical engineering.

He is currently a Professor with Xi'an Jiaotong University. He has authored or coauthored more than 120 SCI journal papers. His research interests include condition monitoring technique, fault diagnosis, and advanced sensor technique for electrical apparatus.

Yi Tang (Senior Member, IEEE) received the B.Eng. degree from Wuhan University, Wuhan, China, in 2007, and the M.Sc. and Ph.D. degrees from the School of Electrical and Electronic Engineering, Nanyang Technological University, Singapore, in 2008 and 2011, respectively, all in electrical engineering.

From 2011 to 2013, he was a Senior Application Engineer with Infineon Technologies Asia Pacific, Singapore. From 2013 to 2015, he was a Postdoctoral Research Fellow with Aalborg University, Aalborg, Denmark. Since March 2015, he has been with Nanyang Technological University, where he is currently an Associate Professor. He is the Cluster Director of the Advanced Power Electronics Research Program, Energy Research Institute, Nanyang Technological University.

Dr. Tang was the receipt of the Infineon Top Inventor Award in 2012, the Early Career Teaching Excellence Award in 2017, the Best Associate Editor Award for IEEE Journal of Emerging and Selected Topics in Power Electronics in 2018, the Outstanding Reviewer for the IEEE TRANSACTIONS ON POWER ELECTRONICS in 2019, and four IEEE Prize Paper Awards. He is an Associate Editor for IEEE TRANSACTIONS ON POWER ELECTRONICS and *IEEE Journal of Emerging and Selected Topics in Power Electronics*.